AGU PUBLICATIONS

JGR

Journal of Geophysical Research: Oceans

RESEARCH ARTICLE

10.1002/2015JC011168

Key Points:
- Remote equatorial forcing explains 89% of the coastal interannual variability
- Coastal trapped waves propagate up to the Benguela Upwelling System (24°S)
- Coastal temperature changes are maximum in the subsurface and result from advection processes

Correspondence to:
M.-L. Bachèlery,
marie-lou.bachelery@legos.obs-mip.fr

Citation:
Bachèlery, M.-L., S. Illig, and I. Dadou (2015), Interannual variability in the South-East Atlantic Ocean, focusing on the Benguela Upwelling System: Remote versus local forcing, *J. Geophys. Res. Oceans*, *120*, doi:10.1002/2015JC011168.

Received 24 JUL 2015
Accepted 10 DEC 2015
Accepted article online 15 DEC 2015

Interannual variability in the South-East Atlantic Ocean, focusing on the Benguela Upwelling System: Remote versus local forcing

Marie-Lou Bachèlery[1], Serena Illig[1,2], and Isabelle Dadou[1]

[1]Laboratoire d'Etudes en Géophysique et Océanographie Spatiales; OMP/LEGOS, Toulouse, France, [2]Department of Oceanography, MARE Institute, University of Cape Town, South Africa

Abstract We investigate the respective roles of equatorial remote (Equatorial Kelvin Waves) and local atmospheric (wind, heat fluxes) forcing on coastal variability in the South-East Atlantic Ocean extending up to the Benguela Upwelling System (BUS) over the 2000–2008 period. We carried out a set of six numerical experiments based on a regional ocean model, that differ only by the prescribed forcing (climatological or total) at surface and lateral boundaries. Results show that at subseasonal timescales (<100 days), the coastal oceanic variability (currents, thermocline, and sea level) is mainly driven by local forcing, while at interannual timescales it is dominated by remote equatorial forcing. At interannual timescales (13–20 months), remotely forced Coastal-Trapped Waves (CTW) propagate poleward along the African southwest coast up to the northern part of the BUS at 24°S, with phase speeds ranging from 0.8 to 1.1 $m.s^{-1}$. We show that two triggering mechanisms limit the southward propagation of CTW: interannual variability of the equatorward Benguela Current prescribed at the model's southern boundary (30°S) and variability of local atmospheric forcing that modulates the magnitude of observed coastal interannual events. When local wind stress forcing is in (out) of phase, the magnitude of the interannual event increases (decreases). Finally, dynamical processes associated with CTW propagations are further investigated using heat budget for two intense interannual events in 2001 and 2003. Results show that significant temperature anomalies (±2°C), that are mostly found in the subsurface, are primarily driven by alongshore and vertical advection processes.

1. Introduction

The four Eastern Boundary Upwelling Systems (EBUS; Benguela-Canaries-California-Humboldt) are among the most productive oceanic ecosystems in the world [*Carr*, 2002; *Carr and Kearns*, 2003; *Chavez and Messié*, 2009], and support vast and diversified marine populations, as well as essential habitats for marine biodiversity. They sustain around 20% of global fisheries for an oceanic surface of only ~1% of the global ocean [*Fréon et al.*, 2009]. This is mainly due to the upwelling of nutrient rich, saline, and cold waters from the subsurface to the sunlit surface layer. Coastal upwelling and Ekman offshore transport [*Strub et al.*, 1998] are forced by dominant surface equatorward wind stress while Ekman pumping is associated with positive wind stress curl [*Albert et al.*, 2010; *Junker et al.*, 2014]. In most EBUS, mesoscale and submesoscale structures (eddies, filaments, and fronts) play an important role on the ocean dynamics. They develop primarily from baroclinic instabilities [*Penven et al.*, 2005], associated with strong horizontal and vertical shear of the alongshore current system. They modify the lateral flux of physical and biogeochemical tracers and induce a strong mixing [*Penven et al.*, 2001; *Shannon et al.*, 2006; *Veitch et al.*, 2009; *Gutknecht et al.*, 2013]. The oceanic circulation in EBUS is also highly sensitive to the connection with equatorial dynamics. The latter is associated with eastward propagation of Equatorial Kelvin Waves (EKW), triggered by trade wind modulations in the western equatorial part of the basin [*Kessler et al.*, 1995; *Cravatte et al.*, 2003; *Illig et al.*, 2004, 2006; *Illig and Dewitte*, 2006; *Rouault et al.*, 2007]. When EKW reach the basin's eastern coast, a significant part of their energy is transmitted poleward as propagating Coastal Trapped Waves (CTW) which contribute to a great amount of coastal oceanic variability [*Brink et al.*, 1978; *Romea and Smith*, 1983; *Clarke*, 1983; *Hormazabal et al.*, 2002; *Polo et al.*, 2008; *Echevin et al.*, 2011, 2014; *Belmadani et al.*, 2012]. In particular, these waves trigger temperature anomalies which could impact atmospheric circulation and rainfall [*Shannon et al.*, 1986; *Rouault et al.*, 2003], and could also have severe effects on nearshore upwelling and biological

productivity. During their propagation, CTW trigger vertical displacements of the thermocline which may modulate surface and subsurface temperature by $\sim\pm2$°C and imprint the Sea Level Anomaly (SLA) by several centimeters [*Pizarro et al*., 2001, 2002; *Leth and Middleton*, 2006; *Rouault et al*., 2009; *Colas et al*., 2008; *Polo et al*., 2008; *Richter et al*., 2010; *Belmadani et al*., 2012]. They may also modulate coastal biogeochemical conditions [*Echevin et al*., 2014]. In order to track their propagation, many recent studies have been focusing on observed satellite SLA and Sea Surface Temperature (SST) signals [*Polo et al*., 2008; *Pizarro et al*., 2001, 2002; *Dewitte et al*., 2008b; *Goubanova et al*., 2013].

When compared to the other three EBUS, the Benguela Upwelling System (BUS) which runs along the southwest coast of Africa from 34°S to 19°S presents some unique characteristics and has been documented to be one of the highest primary fisheries producers in the world [*Carr*, 2002; *Carr and Kearns*, 2003]. It is bordered both to the north and south by two warm water currents: the Angola and Agulhas currents, respectively. These energetic boundaries with strong currents and Eddy Kinetic Energy (EKE) may have large impacts on BUS variability [*Shannon and Nelson*, 1996; *Shillington*, 1998; *Shillington et al*., 2006; *Field and Shillington*, 2005; *Backeberg et al*., 2012]. This ecosystem undergoes recurrent temperature fluctuations, at wide frequency ranges, spanning from submonthly to decadal timescales. To explain these temperature variations, several mechanisms have been put forward at submonthly ($<$30 day) and intraseasonal (30–90 day) timescales. *Goubanova et al*. [2013] did not find any evidence of intraseasonal CTW signature on the satellite SST variability in the BUS during the 2000–2008 period. They instead attribute the submonthly and intraseasonal coastal SST variability off Angola to modulation of alongshore winds, associated with eastward propagating disturbances in the midlatitudes and to Antarctic oscillation variability (or Southern Annular Mode), respectively. In agreement with *Goubanova et al*. [2013], using intraseasonal SLA from altimetry, *Polo et al*. [2008] observed signatures of equatorially forced CTW (with phase speeds between 1.5 and 2.1 m.s^{-1}) along the African coast, but no further south than 12°S. Hence, their results suggest that the connection with remote equatorial variability does not affect the BUS. Note that, both studies were limited by the observed data sets at their disposal. In particular, due to extended masking of satellite data (from land contamination), the identification of CTW signature remains difficult. For longer periods—interannual (18 months) [*Florenchie et al*., 2004] to decadal [*Shannon et al*., 1986] timescales—the strongest SST modulations have been called Benguela Niños [*Shannon et al*., 1986] in reference to poleward propagation of warm water along the equatorial Pacific Ocean and the Peruvian coastline during El Niño events. Benguela Niños are marked by a poleward intrusion of warm equatorial water and reduced upwelling, which diminish nutrient supplies in the euphotic layer. This could lead to drastic consequences for the whole trophic chain [e.g., *Cury and Shannon*, 2004]. Two forcing mechanisms for these Benguela Niños are discussed in the literature. The first relates to zonal wind stress modulation in the western equatorial Atlantic that triggers the EKW which propagate along the equator and subsequently generate CTW along the southwestern coast of Africa. The second mechanism is the disparity in magnitude and position of the South Atlantic Anticyclone that causes wind forcing variations in both regions (along the equator and in the Angola-Benguela Area (ABA, (8°E-coast, 15°S–10°S) [*Shannon and Nelson*, 1996]. At interannual timescales, based on ocean-atmosphere coupled model analysis, *Richter et al*. [2010] have suggested that meridional winds along the southwestern coast of Africa contribute substantially to interannual SST variability. However, numerous studies [*Philander*, 1986; *Florenchie et al*., 2003, 2004; *Huang et al*., 2004; *Reason et al*., 2006; *Hu and Huang* 2007; *Rouault et al*., 2009; *Lübbecke et al*., 2010] have discussed remote equatorial influence on the Benguela Niño and point out the strong connection between oceanic variability in the ABA and the equatorial Atlantic Ocean.

The aim of this paper is to investigate the contribution of remote equatorial forcing versus local forcing (wind stress and surface heat fluxes) on oceanic variability along the African coast in the South-East Atlantic Ocean, with a focus on the Benguela Upwelling System. In particular, we aim to quantify the most poleward latitude to which CTW can propagate and impact oceanic variability along the coast of southwestern Africa.

We focus on the interannual timescales, given that at these frequencies altimetry SLA provides a coherent signature at the equator and along the African coast. This is illustrating on Figure 1 that presents the energy spectra of the Anomalies (A) of SLA relative to the seasonal cycle (see section 2.3 for filtering methodology) estimated from AVISO data (see section 2 for data description) as a function of longitude along the equator, and latitude along the southwestern coast of Africa. It highlights that compared to the intraseasonal signal, interannual periods ($\sim$380–520 days) provide a continuous and significant signal from the center of the

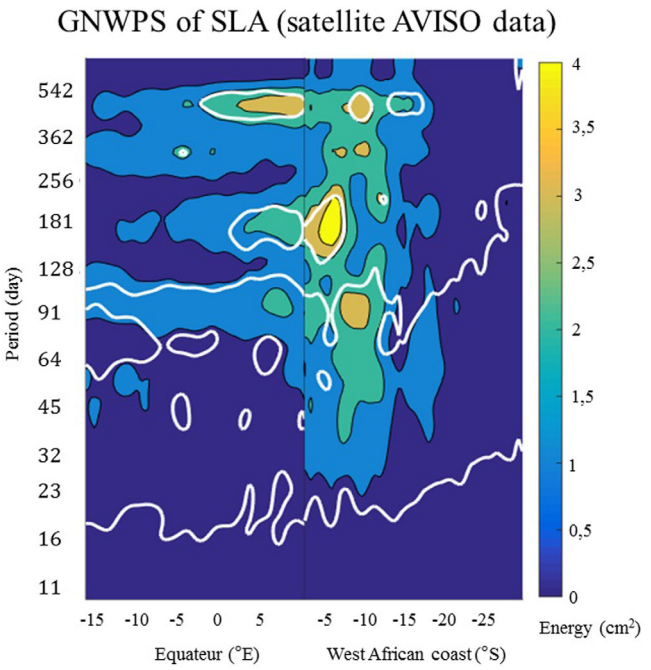

Figure 1. Global Normalized Wavelet Power Spectrum (GNWPS) of SLA Anomalies (A) relative to the seasonal cycle along the equator (left-side plot) and along the African southwest coast (right-side plot) for the 2000–2008 period for satellite data (AVISO) averaged every 5 days. Black contour interval is 1 cm^2. White contour corresponds to significant values at 90% confidence level.

equatorial basin as far as 17°S along the African coast. Our approach is based on numerical experimentation with a regional ocean model. This approach overcomes the limitation encountered by *Polo et al*. [2008] and *Goubanova et al*. [2013] as well as providing an evaluation of subsurface variability, where the CTW signature is expected to be more intense than in the surface layer [*Brink*, 1982*; Lübbecke et al*., 2010]. Like *Illig et al*. [2014], we perform sensitivity experiments in order to isolate remote forcing from the local forcing contribution, and identify their respective impacts on physical oceanic dynamics (temperature, SLA, currents, density, and heat budget).

The paper is structured as follows: the next section describes observed data sets and reanalysis as well as the methodology used in this study. Section 3 presents the regional oceanic model, as well as a description of numerical experiments carried out for sensitivity analysis. Note that the estimation of the model performances against in situ data is provided in Appendix A. Sections 4 and 5 are devoted to result analysis. First, we quantify the contributions of remote versus local forcing to the South-East Atlantic oceanic variability and we analyze the properties associated with poleward propagating CTW at interannual timescales. We discuss the most southward latitude at which CTW signatures can be observed in the surface and subsurface layers. Following this, we evaluate CTW characteristics along the African coast as far as the Benguela Upwelling System. We quantify the associated thermodynamical processes based on analysis of online heat budget. Finally, concluding remarks and perspectives to this work are given in section 6.

2. Observation, Reanalysis Data Sets, and Methods

For forcing and analysis of model simulations performed in this study, different satellite and reanalysis outputs are used.

2.1. Satellite Data Sets

2.1.1. Wind Stress

We use gridded Sea Winds scatterometer zonal and meridional wind stress observations from NASA satellite QuikSCAT [*Liu et al*., 1998]. This data are available over the 2000–2008 period as daily means with a resolution of 0.5° × 0.5°, through the French ERS Processing and Archiving Facility CERSAT (http://cersat.ifremer.fr). In near coastal regions, data are masked and not available within a range of 25 km to the coast due to land contamination. Note that for modeling purposes an extrapolation of momentum fluxes was performed within QuikSCAT blind zone using a simple near-neighbor procedure.

2.1.2. Sea Level Anomalies (SLA)

We use the gridded AVISO combined product for SLA, provided by the Ocean Topography Experiment TOPEX/Poseidon/Jason and the European Remote Sensing Satellite ERS-1/2 data sets. We used AVISO data from January 2000 up to December 2008 with a daily frequency on a 1/3° Mercator grid [*Le Traon et al*., 1998; *Ducet et al*., 2000].

2.2. Reanalysis Data Sets

2.2.1. Oceanic Reanalysis

The outputs of the Simple Ocean Data Assimilation reanalysis (SODA, version 2.1.6) are used at the open boundaries of our model configuration (see sections 2.1 and 2.3). SODA provides a set of estimated ocean states based on numerical simulations with data assimilation from the 1994 World Ocean Atlas (WOA-94); other hydrography data; SST; altimetry sea level; and data from NODC, NCEP, and TOGA/TAO over the 1958–2008 period. Additionally, SODA is driven by surface winds from the European Center for Medium-Range Weather Forecasts ERA-40 and ERA-Interim reanalysis data. See *Carton et al*. [2000], *Carton and Giese* [2008], and *Carton et al*. [2005] for more details on the model and data assimilation procedures. Homogeneous temporal series of 5 day averages of temperature, salinity, sea level, and currents, with a horizontal resolution of $0.5^\circ \times 0.5^\circ$ and 40 verticals levels are available at http://www.atmos.umd.edu/~ocean/data.html.

2.2.2. Atmospheric Reanalysis

For our model configuration, oceanic surface heat fluxes and Sea Surface Salinity (SSS) are provided by the National Center of Environmental Prediction-Climate Forecast System Reanalysis (NCEP-CFSR) [*Saha et al*., 2010]. NCEP-CFSR outputs are available on a $0.5^\circ \times 0.5^\circ$ horizontal grid at different temporal resolutions (from hourly to monthly) over the 31 year period extending from 1979 to 2009. CFSR is a coupled (ocean/atmosphere/land surface/sea ice) data assimilation system using observed SST, temperature, and salinity profiles from MBT, XBT, CTD, Argo, and TAO. This product is a significant upgrade from the older reanalysis (NCEP-R1, NCEP-R2) done at NCEP [*Kalnay et al*., 1996; *Kanamitsu et al*., 2002]. In particular, the model was improved by adding finer atmospheric resolution, an advanced assimilation scheme, an atmosphere-land-ocean-sea ice coupling, and the assimilation of satellite radiance.

2.3. Methods and Tools

2.3.1. Filtering Procedure

In the tropical Atlantic Ocean, salient variables are mostly dominated by the annual and semiannual cycles over the equatorial sector and along the African coast [*Wilson and Adamec*, 2002; *Schouten et al*., 2005]. In order to retain only the interannual variability, we use methodology from *Mosquera-Vásquez et al*. [2014]:

1. Anomalies (A) are primarily considered as departures from the monthly climatology. To do so, we first estimate the monthly climatology over the 2000–2008 period and interpolate it onto the original 5 day resolution using cubic splines. Then, this monthly climatology at 5 day resolution is subtracted from the original data. This filter is applied to remove the seasonal cycle (annual and semiannual frequencies) while subseasonal (submonthly and intraseasonal) and interannual variabilities survive in the filtered time-series.
2. From these anomalies (A), we extract the interannual frequencies (IA): to do so, we estimate the monthly means of the Anomalies (A), which are then smoothed using a 1-2-1 filter (1-2-1 running weighted average) and interpolated back onto the 5 day original resolution using cubic splines. The spectral characteristics of this low pass filter were examined using a Gaussian white noise. The resulting transfer function depicts a -10 dB, -3 dB, -1 dB attenuation (10%, 50% 79% of the input power survives) at 100 d^{-1}, 168 d^{-1}, and 283 d^{-1}.

Subseasonal anomalies are defined as the complementary signal to the interannual anomalies: They are calculated by subtracting the IA from A [see *Goubanova et al*., 2013; *Illig et al*. 2014].

2.3.2. Wavelet Analysis

The wavelet analysis is a powerful tool, commonly used in geophysics for detecting time-frequency variations within time-series. A detailed description of the wavelet analysis used in this study can be found in *Torrence and Compo* [1998]. In order to describe spatial and temporal characteristics of EKW and CTW, we have chosen to use a 1-D (time) wavelet analysis with a continuous wavelet transform based on the Morlet function ($\omega_0 = 6$). In order to compare the wavelet spectrum's amplitude at different frequencies, we estimated the Normalized Wavelet Power Spectrum (NWPS) using the method described in *Goubanova et al*. [2013]. Also, following *Torrence and Compo* [1998], significance levels (at 95%) are determined from the $\chi 2$ distribution calculated from the autocorrelated time-series at lag -1 (5 days) and lag -2 (-10 days).

2.3.3. EOF Analysis

In order to extract the dominant mode of interannual variability, we apply a classic Empirical Orthogonal Function (EOF) decomposition [*Toumazou and Cretaux*, 2001] to the data set over the 2000–2008 period.

We normalized the EOF spatial patterns (here after referred to as EOFs) and the associated time-series (Principal Component or PC) so that the maximum of each EOF is equal to one.

2.3.4. Vertical Mode Decomposition

SODA model outputs are further used to derive an estimate of EKW contributions based on a modal decomposition of variability (pressure and zonal current), which is not possible to obtain from available surface observations. Contributions of the first three EKW modes (the most energetic at interannual timescales) are derived following the method described in *Illig et al*. [2004]. This method consists in deriving vertical modes from seasonally and zonally slow-varying stratification over which pressure and zonal current anomalies are projected. This provides the baroclinic mode contribution to sea level and zonal current which are then projected onto the theoretical meridional structures of EKW, accounting explicitly for the coastal boundary near the equator in the Gulf of Guinea [*Cane and Sarachik*, 1979]. EKW are expressed in terms of amplitude of their contribution to sea level anomalies. This method using SODA output was shown to be efficient in capturing the salient features of the propagating characteristics (phase speed and amplitude) of EKW contributions for both the Pacific [*Dewitte et al*., 2008a,b] and Atlantic [*Goubanova et al*., 2013] Oceans.

3. Regional Oceanic Simulations

In order to quantify the respective roles of boundary forcing: namely, remote equatorial forcing and local atmospheric forcing on the variability along the southwestern coast of Africa, we use a regional oceanic physical model of the South-East Atlantic Ocean. The following section is devoted to describing the model configuration and various experiments that were performed. A summarized analysis of how the model reference simulation performed with regards to mean state and interannual variability is provided in Appendix A.

3.1. Regional Ocean Model Configuration

The Regional Ocean Modeling System (ROMS—*Haidvogel et al*. [2000]; *Shchepetkin and McWilliams* [2003, 2005]) is used to simulate the salient features of large and regional-scale circulation patterns in the South-East Atlantic region. ROMS is a free surface, topography-following coordinate model with a split-explicit time stepping that solves primitive equations based on Boussinesq and hydrostatic approximations. In this study, we use the AGRIF (Adaptive Grid Refinement in Fortran, *Debreu et al*. [2008]) version of ROMS (version 3.0) which is freely available at http://www.romsagrif.org and is regularly improved and updated by its developers [*Penven et al*., 2006a; *Debreu et al*., 2012]. Subgrid-scale vertical mixing is parameterized using a K-Profile Parameterization (KPP) boundary layer scheme [*Large et al*., 1994]. For the tracers, we used the horizontal third-order upstream advection scheme with split and rotated diffusion [*Marchesiello et al*., 2009; *Lemarié et al*., 2012], recommended in realistic applications to preserve water masses.

The domain covers the region between 30°S and 7°N, spanning from 10°W to the southwestern coast of the African continent (Figure A1a in Appendix A). The horizontal resolution is 1/12° (∼9.25 km at the equator) with 37 sigma vertical levels, which are stretched in the surface layer. As shown by *Penven et al*. [2006a,b], this configuration is suitable to correctly resolve coastal upwelling processes and most mesoscale dynamics. Indeed, the wavelength associated with the first baroclinic Rossby Radius in the region along the coast of interest varies from ∼250 km near the equator to 20 km at 30°S [*Houry et al*., 1987; *Chelton et al*., 1998].

Within this configuration, the western and southern borders are open using a mixed radiation-nudging scheme [*Marchesiello et al*., 2001] with temperature, salinity, sea level, and currents fields derived from SODA reanalysis (see section 2.2), while the northern and eastern boundaries remain closed. Our choice for using SODA at our model Open Boundary Conditions (OBCs) was motivated by its skills in correctly simulating the EKW propagating characteristics, along with the vertical structure of temperature, pressure, and currents (see section 2.3). Topography is derived from the GEBCO_08 global elevation database at 30 arc-second spatial resolution (http://www.gebco.net). Note also that a linear adjustment of model bathymetry to SODA bathymetry is made within a 2° band in order to insure continuity of both model solutions (SODA and ROMS). Wind stress forcing comes from daily QuikSCAT gridded data, while for surface heat flux forcing we used daily averages of atmospheric NCEP/CFSR reanalysis using bulk formulations [*Fairall et al*., 1996]. As no river discharges are taken into account in our ROMS simulations, modeled SSS is restored to the SSS from NCEP/CFSR ocean reanalysis (see section 2.2). For initial conditions, SODA potential temperature, salinity, horizontal current, and Sea Surface Height (SSH) of the January 2000 year fields were used.

Table 1. Description of ROMS Experiments: Name, Open Boundary Conditions (OBCs), QuikSCAT Wind Stress Forcing Specification and Heat/Fresh-Water Flux Forcing Specification

Name	OBC	Wind Stress	Heat/Water Fluxes
$ROMS^{REF}$	Total	Total	Total
$ROMS^{EQ}$	Total, between 10°N–10°S	Climatological	Climatological
$ROMS^{EQ+SOUTH}$	Total	Climatological	Climatological
$ROMS^{LOCAL}$	Climatological	Total	Total
$ROMS^{LOCAL\_SOUTH}$	Climatological	Total, except North of 4°S	Total, except North of 4°S
$ROMS^{CLIM}$	Climatological	Climatological	Climatological

The model reaches an equilibrium state after 5 years of spin-up, performed using climatological forcing (OBC and surface forcing) estimated over the 2000–2008 period. Then, the simulation is performed over a 9 year period spanning from 2000 to 2008, during which 5 day averages of model state variables (temperature, salinity, currents), as well as temperature budget terms and daily averages of SSH were stored. For the interannual variability study, which is the focus of this paper, 9 years of simulation is a short period. However, thanks to our filtering methodology, it is sufficient to represent known extreme IA events (2001—*Rouault et al*. [2007]; 2006/2007—*Marin et al*. [2009]). Moreover, it corresponds to available QuikSCAT data which provides the best model estimates and allows us to conserve consistent atmospheric forcing for the entire time-series.

Performance of the reference simulation ($ROMS^{REF}$) is presented in Appendix A. Results show a realistic simulation of the South-East Atlantic Ocean mean state and interannual variability. Thus, we gain confidence in use of our model outputs and carry out sensitivity experiments regarding model forcing to study the influence of CTW along the southwest coast of Africa and their impact in the Benguela Upwelling System.

3.2. Numerical Experiments

A set of six numerical experiments were carried out in order to identify the oceanic response in the southeastern part of the Atlantic Ocean, to different forcing conditions: wind stress, heat flux, and equatorial remote forcing (EKW). Therefore, our ROMS experiments differ only by forcing at the model boundaries: OBC and surface atmospheric forcing (wind stress and heat fluxes) which are either climatological or real time (see Table 1 for a summary of these numerical experiments). First, we define the reference simulation described in section 3.1: $ROMS^{REF}$ simulation is the most realistic experiment performed using 5 day SODA at the ocean boundaries, daily QuikSCAT wind stress, and daily NCEP-CFSR atmospheric forcing. Then, with the aim of isolating the impact of EKW along the African southwest coast from local atmospheric forcing (wind stress and heat fluxes), we define a second simulation, labeled $ROMS^{EQ}$, in which the 5 day SODA reanalysis is used at the western boundary between 10°S and 7°N, while the remaining OBC and surface atmospheric forcing (wind stress and heat fluxes) are set to climatology. Within this configuration, at interannual timescales, the South-East Atlantic regional circulation is impacted by remote equatorial forcing (and internal model variability) and hence CTW are expected to propagate along the southwest coast of Africa. Next, a sensitivity experiment to the southern boundary dynamics is performed (cf. section 4.3): $ROMS^{EQ+SOUTH}$ and is based on $ROMS^{EQ}$ configuration except that we apply real time forcing (5 day SODA) at all OBCs. Two configurations have been designed in order to quantify atmospheric forcing (wind stress and heat fluxes) influence on interannual South-East Atlantic Ocean variability. The first configuration is $ROMS^{LOCAL}$ and is a paired experiment to $ROMS^{EQ}$ in which OBC's are climatological (i.e., no remote equatorial forcing), while daily surface forcing (wind stress and heat fluxes) is used over the entire domain. Thus, in $ROMS^{LOCAL}$, only atmospheric effects are expected to trigger interannual variability (as well as intrinsic variability). However, even if most EKW are forced in the western equatorial Atlantic [*Zebiak*, 1993; *Illig et al*., 2004, 2006; *Illig and Dewitte*, 2006] due to the design of our model configuration whose western boundary is at 10°W, wind-stress fluctuations in the Gulf of Guinea can also force eastward equatorial Kelvin Waves, which in turn can trigger poleward CTW. In the framework of the present study, this mechanism has to be considered as remote forcing. In order to quantify the importance of EKW forced in the Gulf of Guinea in $ROMS^{LOCAL}$, another sensitivity experiment was carried out to limit generation of EKW in the Gulf of Guinea (cf. section 4.3): $ROMS^{LOCAL\_SOUTH}$ presents the same characteristics as $ROMS^{LOCAL}$, except that north of 4°S climatological wind stress and heat flux forcing have been prescribed. Note that a linear adjustment was made on a 2° width band (from 4°S to 6°S) to insure continuity between both forcing (climatological and total) and reduce erroneous wind

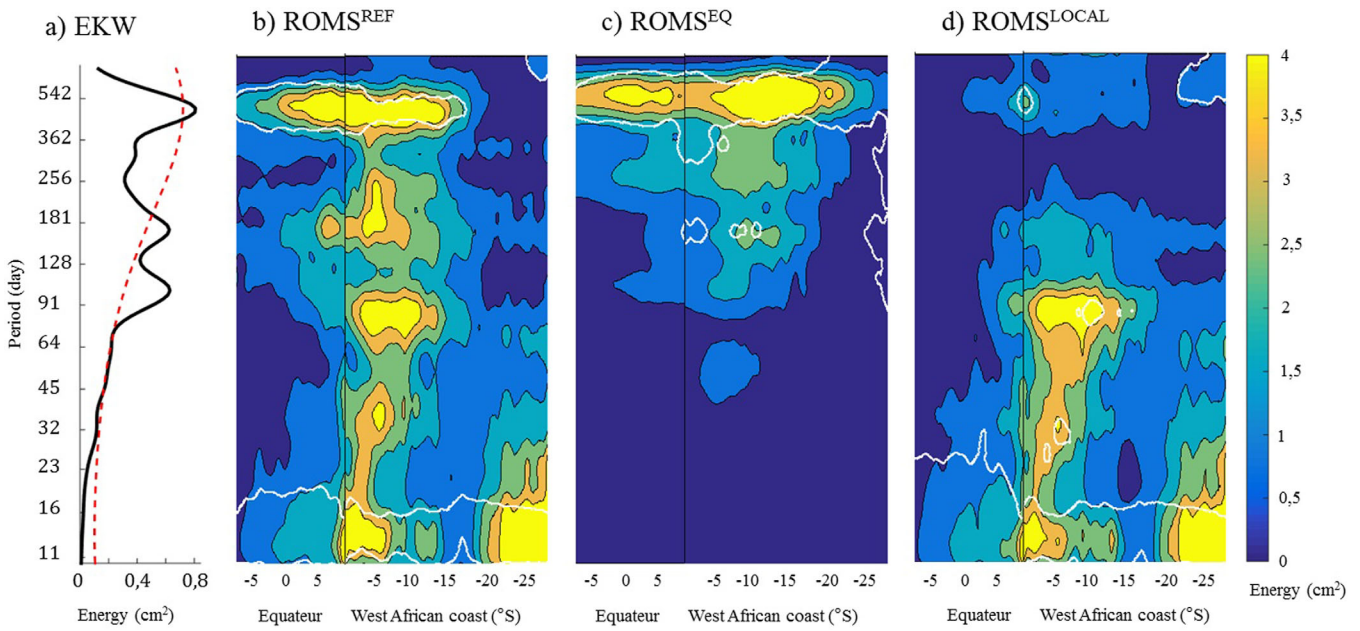

Figure 2. Global Normalized Wavelet Power Spectrum (GNWPS) for the 2000–2008 period. (a) Equatorial Kelvin Wave (EKW) Anomalies (A, relative to the seasonal cycle) contribution to the sum of the three gravest baroclinic mode SLA at [0°N; 10°W]. (b–d) Same as Figure 1: SLA Anomalies (A) along the equator (averaged between 1°S and 1°N) and along the African southwest coast (averaged within the 0.5°-width coastal band) for (b) ROMS^{REF}, (c) ROMS^{EQ}, and (d) ROMS^{LOCAL} simulations. Black contour interval is 0.8 cm^2. The red-dashed line (Figure 2a) and white contour (Figures 2b–2d) correspond to significant values at 90% confidence level.

stress. In this simulation, EKW cannot be forced locally at the equator in the Gulf of Guinea and so, in comparison to ROMS^{LOCAL}, only local atmospheric and internal model dynamics affect the interannual variability along the African southwest coast. A final ROMS^{CLIM} experiment was designed to quantify the model's internal dynamics (nonlinearity) and the seasonal and mesoscale oceanic variability. We used climatological atmospheric forcing (wind stress and heat fluxes) as well as climatological OBCs.

4. Remote Versus Local Forcing: Results and Discussion

In this section, we investigate the contribution of remote equatorial forcing versus local forcing on South-East Atlantic oceanic variability with special interest in the properties of poleward CTW propagations. In particular, we aim to determine the most poleward latitude along the African coast at which the CTW signature can be observed in surface and subsurface layers.

4.1. Relative Contribution to Forcing

Under the linearity hypothesis, outputs of our model experiments can be used to quantify the impact of remote equatorial forcing versus local forcing on ocean dynamics. To get an overview of the equatorial signal transmission from the equator area to the southwestern coast of Africa as a function of frequency ranges, Figures 2b and 2d display the Normalized Global Wavelet Spectrum (NGWS) of Anomalies (A) of SLA (cf. Section 2.3 for the filtering methodology) along the equator and along the southwest coast of Africa for reference (ROMS^{REF}), remote (ROMS^{EQ}), and local (ROMS^{LOCAL}) simulations (Table 1). Note that the energy spectrum of the ROMS^{CLIM} experiment (not shown) is much weaker than the one of the other five simulations and for all frequencies from submonthly to interannual timescales. For example, the ratio of the NGWS averaged along the African southwest coast (30°S–0°N) between ROMS^{CLIM} and ROMS^{REF} is lower than 6% for all the periods from 10 to 630 days. Figure 2 reveals that results obtained for the reference simulation (Figure 2b) are similar to that obtained using satellite data (Figure 1) with strong energetic signals centered around 100, 181, and 490 day frequencies. Comparison between the three model experiments shows that along the southwest coast of Africa, the energy spectra of ROMS^{EQ} and ROMS^{LOCAL} can almost be linearly added up to reconstitute the reference signal (ROMS^{REF}). Results show that at subseasonal timescales (10–20 days and 80–105 days), the SLA variability is primarily driven by local atmospheric forcing with a ratio of the NGWS averaged along the southwest coast of Africa (30°S–0°N) between ROMS^{LOCAL} (ROMS^{EQ}) and

ROMS^{REF} larger (lower) than 99% (17%). In agreement with *Polo et al*., [2008], ROMS^{EQ} exhibits some variability at intraseasonal time scales (at 45 and 95 days) until 12°S. However, the energy level is significantly weaker than ROMS^{LOCAL}. This is most likely due to the design of our configuration (cf. section 3.2), in which wind-stress fluctuations in the Gulf of Guinea force EKW and then CTW. Further south, our results are in agreement with *Goubanova et al*. [2013] who showed that subseasonal (submonthly and intraseasonal) SST variability in the central BUS is mainly modulated by local forcing (wind stress). They found no evidence to support the hypothesis that subseasonal Equatorial Kelvin Waves (EKW) contribute to subseasonal SST variability in the BUS. Conversely, at interannual timescales (between 380 and 540 days), experimentation with ROMS reveals that coastal SLA variability along the African coast is mostly explained by equatorial forcing (Figure 2), since the NGWS ratio between ROMS^{EQ} and ROMS^{REF} at interannual frequencies is larger than 89%, while it remains lower than 29% for ROMS^{LOCAL}. This is in agreement with *Lübbecke et al*. [2010] who demonstrated that remote forcing has a higher contribution than wind-driven local upwelling anomalies for warm event generation. It also supports the results of *Florenchie et al*. [2003, 2004] and *Rouault et al*. [2007] who suggest that warm events off Angola in the ABA are remotely forced from equatorial EKW propagation. They explained that interannual SST anomalies associated with Benguela Niños are not generated locally but are driven by relaxation of the trade winds in the western part of the equatorial Atlantic basin. In this context, we further examined the variability of EKW contributions by estimating the energy spectra of the sum of the three gravest baroclinic mode EKW contributions to the SLA at [10°W; 0°N] based on SODA outputs (see section 2.3 for more details about EKW decomposition). The associated NGWS is displayed in Figure 2a and reveals the presence of two major periods of variability. Energy peaks at intraseasonal timescales (between 90–110 and ∼150 days) were identified in *Goubanova et al*. [2013], while the most energetic peak at interannual scales (390–550 days i.e.,13–18 months) matches well with the interannual energy peaks obtained in ROMS^{EQ} (Figure 2b), ROMS^{REF} (Figure 2a), and in the observation analysis (Figure 1). This interannual frequency peak is also coherent with the main interannual frequency of Benguela Niño events at ∼18 months [*Florenchie et al*. 2004]. Note that, Figure 2 as Figure 1 contains substantial energy at semiannual and annual periods which likely results from the interannual modulation of the annual and semiannual cycle. This is in agreement with the results of *Polo et al*. [2008] that showed that the intraseasonal variability is significantly dependent on the seasonal cycle with more positive propagations observed during the downwelling season (from September to February) and negative propagations detected during the upwelling season (March to August).

In summary, these results indicate that remote equatorial forcing is the main process driving SLA variability along the equator and the southwestern coast of Africa at interannual frequencies. In the following section, we investigate in more detail the interannual coastal oceanic dynamics, and in particular refine the estimation of the most poleward latitude up to which remote equatorial forcing can impact interannual coastal variability.

4.2. Poleward CTW Propagation in the Surface and Subsurface Layers

To begin with, interannual coastal oceanic dynamics are investigated in the surface layer by regarding the correlation between interannual SLA (SLIA; see section 2.3 for details on the filtering methodology) of ROMS^{REF} and AVISO data (Figure 3). Agreement between model and observations is statistically significant, especially along the equatorial wave guide and along the southwest coast of Africa up to 24°S. This highlights how far South the equatorially forced signal stay coherent and emphasizes where the variability is influenced by coastal trapped waves. This hypothesis has been further investigated using baroclinic mode EKW contribution to interannual SLA at 10°W-Equator (see section 2.3 for details on vertical mode decomposition) and ROMS^{REF} coastal Interannual SLA (SLIA). Figure 4a displays the lagged correlation coefficient between the sum of the three gravest baroclinic mode EKW contributions to SLIA at [10°W; 0°N] and ROMS-^{REF} SLIA taken at each point along the Southwest African Coast. The correlation coefficient is significant from 0°S up to 17°S with correlation coefficients between 0.5 and 0.6. Subsequently, further south, this coefficient decreases and becomes nonsignificant upon reaching 0.38 at 20°S. Based on lag (Figure 4a), the mean coastal propagation phase speed along the southwest coast of Africa is estimated at 1.09 m.s^{-1}. We then investigate the distinct contribution of each EKW mode to SLIA (Figure 4b). In agreement with *Illig et al*. [2004], along the equator, from 10°W to 0°E, both second and first baroclinic mode contribution to Interannual SLA are dominant, while east of 2°E the third baroclinic mode becomes the most energetic mode due to shallower and more stratified mean thermocline (not shown). Along the southwest coast of Africa, the SLIA variability correlates best with the third baroclinic mode at [10°W; 0°N] from 0°S to 17°S

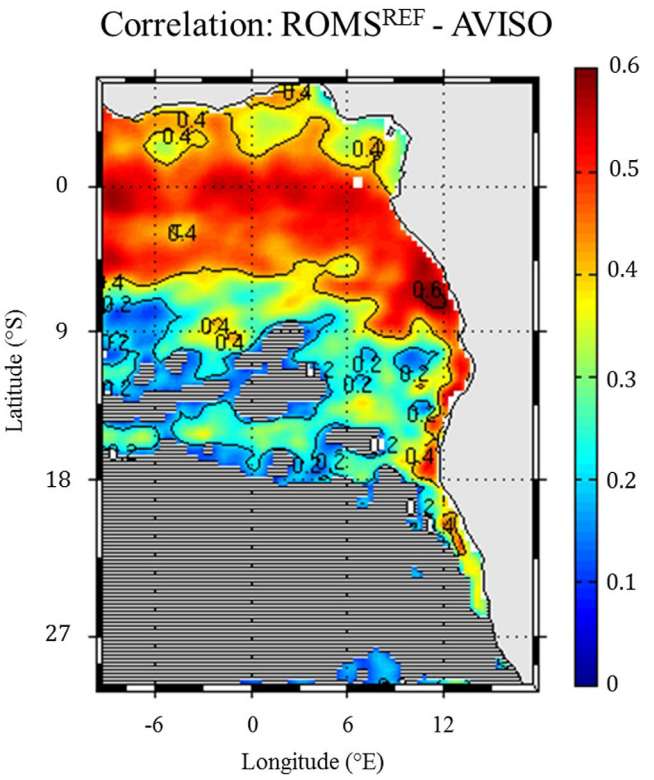

Figure 3. Correlation map between 5 day-averaged ROMS^{REF} Sea Level Interannual Anomalies (SLIA) and observed SLIA from AVISO over the 2000–2008 period. The black and white ribs denote nonsignificant correlations (at 95% confidence level).

(correlation coefficient larger than 0.4). South of 17°S, the coastal variability shares more temporal characteristics with the first baroclinic mode at [10°W; 0°N], with correlation coefficient equals to 0.42 at 20°S. In summary, these results indicate that remote equatorial forcing (EKW) triggers poleward CTW [*Brink et al*., 1978; *Romea and Smith*, 1983; *Clarke*, 1983; *Hormazabal et al*., 2002; *Polo et al*., 2008; *Echevin et al*., 2011, 2014; *Belmadani et al*., 2012] which induces significant coastal variability on the sea level variability at interannual frequencies along the equator and west coast of Africa up to ~17°S. This latitude is north of the BUS (located between 19°S and 34°S). Consequently, the CTW signature as observed from altimetry does not reach the BUS. However, as CTW propagation is associated with vertical displacements of the thermocline, in the following section our analysis focuses on subsurface variability, which might be detectable further South.

To access subsurface oceanic interannual variability, we used a method inspired from that described in *Belmadani et al*. [2012]. Empirical Orthogonal Functions (EOFs) are computed over cross-shore vertical sections of interannual alongshore currents and density anomalies every 1° of latitude along the western African coast. We aim to isolate variability exclusively associated with CTW dynamics, and reduce contamination associated with the extratropical Rossby Waves that radiate offshore from the coast. To do so, for each latitude, the EOF analysis is performed on a cross-shore section width equal to the first Rossby radius. Note that, in agreement with *Belmadani et al*. [2012], the results do not exhibit significant sensitivity to EOF cross-shore section width. The EOFs spatial pattern and associated time-series (Principal Components-PCs) are analyzed in order to identify the dominant mode of interannual variability in the subsurface and to describe its characteristics along the African coast. Since the conclusions drawn from the analysis of coastal density and alongshore currents remain equivalent, we only present here the analysis on density interannual anomalies (IA). To illustrate the mode of variability captured by analysis of interannual density anomalies, Figure 5 shows the dominant EOF spatial patterns for the three simulations ROMS^{REF}, ROMS^{EQ}, and ROMS^{LOCAL} at 15°S. Note that, in order to be able to compare the PCs from one latitude to another, we have chosen a normalization of the spatial pattern such as the maximum density anomalies within the thermocline are equal to 1 (cf. section 2.3). This statistically dominant first mode (ROMS^{REF}: 84%, ROMS^{EQ}: 82%, ROMS^{LOCAL}: 89% of the total variance) presents a significant alongshore variability, maximum in subsurface between a depth of 10 and 45 m. For each latitude (not shown), the dominant mode of variability peaks between the surface and the Mixed Layer Depth (MLD) in ROMS^{LOCAL}, while it extends deeper in ROMS^{EQ}. To quantify the impact of different forcing on interannual coastal density variability, we have estimated the RMS of the time-series associated with the spatial patterns presented in Figure 5 (see RMS values in the lower right corner). It shows that the variability is stronger for ROMS^{EQ}, with a value of 0.36 at 15°S (ROMS^{REF}: 0.31 and ROMS^{LOCAL}: 0.24). Similar results were obtained from 5°S to 30°S.

Subsurface propagation properties of interannual CTW (IA) are investigated through the study of lag correlation between PCs associated with the dominant EOF at each latitude (every 1°) along the southwest coast

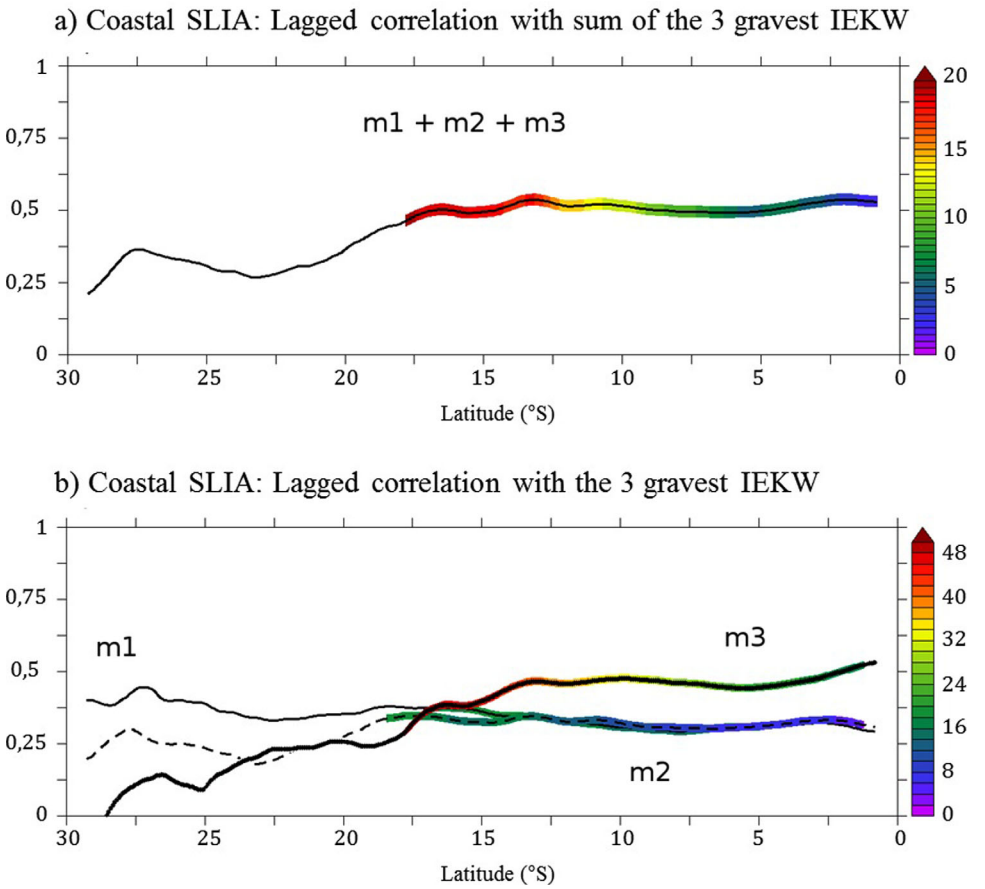

Figure 4. Maximum lagged correlation between coastal Sea Level Interannual Anomalies (SLIA) along the African coast from the ROMS^{REF} simulation and the Interannual Equatorial Kelvin Wave (IEKW) contribution to the first three baroclinic mode SLIA at [0°N; 10°W] estimated from SODA Reanalysis. Significant correlation (at 95% confidence level) associated with increasing lag (days) is specified by color shading. Positive values mean that IEKW signal leads. (a) For the IEKW contribution to the sum of the first three baroclinic modes (m1 + m2 + m3). (b) The plain thin line corresponds to the interannual equatorial Kelvin wave contribution to the first baroclinic mode (m1), the dashed thin line to the second baroclinic mode (m2), and the large plain line corresponds to the third baroclinic mode (m3).

of Africa (until 30°S) and the one estimated at 8°S (Figure 6). Note that similar results were obtained using any reference between 5°S and 20°S. Also, in Figure 6, shading indicates positive correlation with a significance level larger than 95% (*p*-value statistical test from *Best and Roberts* [1975]). Signatures of poleward propagations are clearly visible for ROMS^{REF} and ROMS^{EQ} simulations (Figures 6a and 6b): at each latitude along the African coast, the maximum correlation is associated with increasing time-lags when moving poleward. Conversely, for the ROMS^{LOCAL} experiment, we cannot identify any propagative signal between 5°S and 18°S (Figure 6c). More precisely, we capture an instantaneous forcing of the vertical stratification, with a noisy signal between 18°S and 30°S. In addition, the 95% significance level of correlation values suggests that CTW signature can be detected further poleward in the subsurface layer than in the SLA analysis. Figure 5a shows that they can impact stratification variability as far as 24°S in the ROMS^{REF} simulation.

Using results presented in Figure 6, we have further assessed the average phase speed associated with ROMS^{REF} and ROMS^{EQ} density propagation by estimating the slope of the least square best fit to the points with maximum correlation at each latitude along the southwest coast of Africa. The results provide values of 0.85 and 0.89 m.s^{-1}, respectively. Thus, estimated phase speeds using interannual SLA and density fields are both slower than theoretical phase speeds of the first and second baroclinic EKW mode in the tropical Atlantic Ocean (∼2.4 and ∼1.4 m.s^{-1}) [*Katz*, 1997; *Delecluse et al*., 1994; *Illig et al*., 2004; *Schouten et al*., 2005], and are in better agreement with the third baroclinic EKW modes (∼0.8m.s^{-1}) [*Illig et al*., 2004; *Schouten et al*., 2005]. This is consistent with our results presented in Figure 5 and this suggests that the interannual variability along the African southwest coast is associated with a third baroclinic mode of CTW. Interestingly, modeled phase speeds in our study are also slower than phase speeds estimated along the

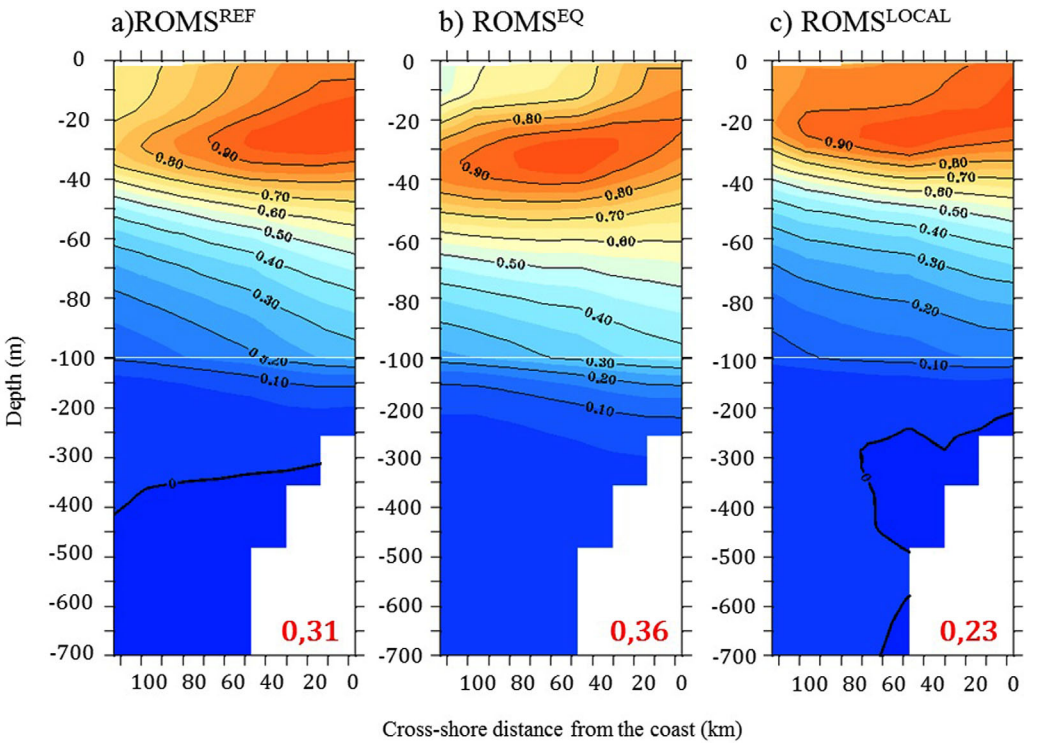

Figure 5. Spatial patterns of the first Empirical Orthogonal Function (EOF) of the interannual alongshore density field (IA) over the cross-shore section at 15°S for the three simulations ROMS^{REF}, ROMS^{EQ}, and ROMS^{LOCAL}, respectively, as a function of the distance from the coast (km) and depth (m). Note that, spatial patterns have been normalized, such as their local maximum is equal to 1. Values listed in the right lower corner (in red) correspond to the associated time-series Root Mean Square in kg.m^{-3}.

equator and the western coast of Africa as far as 12°S by *Polo et al.* [2008] (∼1.5–2.1 m.s^{-1}, respectively), and along the Peru-Chile coast by *Clarke and Ahmed* [1999] and *Belmadani et al.* [2012] (2.89 ± 0.04 m.s^{-1}and between 2.17–2.60 m.s^{-1}, respectively). The discrepancy may be due to dependence of the phase speed on the topography morphology (shelf/slope) and on bottom friction. Long-wave phase speed increases in shallow areas [*Shaffer et al.*, 1997], while it decreases with the bottom friction coefficient [*Clarke and Ahmed*, 1999], consistent with scattering of CTW energy of the first baroclinic mode into higher order modes, which propagate more slowly. For example, along the southwest coast of Africa the shelf slope is gentler than in the Peru-Chile region and hence, the friction effect may be much stronger, contributing to a slower phase speed. More importantly, the timescales examined by *Polo et al.* [2008] and *Belmadani et al.* [2012] focused on intraseasonal variability, whereas we focus on interannual variability. *Clarke and Ahmed* [1999] used modeling framework to show that lower frequencies enhance the dynamical contribution of bottom friction and thus the phase speed decreases. As a result, phase speed at interannual frequencies is expected to be slower than that at intraseasonal frequencies for the same baroclinic mode. We tested this hypothesis by calculating the phase speed associated with intraseasonal events for the ROMS^{EQ} simulation. The obtained phase speed equals 1.79 m.s^{-1}, which is larger than our value estimated for interannual frequencies, and is in better agreement with the results of *Clarke and Ahmed* [1999] and *Polo et al.* [2008]. Note that, the estimation of the phase speed differs in function of the parameter used for the estimation: tracer (temperature, salinity) or dynamical field (thermocline depth, sea level).As in *Rouault et al.* [2007], we observe southward spreading of water from the equator (see section 5).The speed associated with water mass spreading or tracer's advection is superimposed to the linear wave propagation speed. This may explain the difference between phase speed obtained with interannual SLA and density field.

In summary, these results clearly demonstrate the presence of equatorially forced poleward propagating CTW along the southwest coast of Africa at interannual frequencies (periodicity of 400–520 days) in ROMS-^{REF} as far as 24°S. Through the comparison between our sensibility experiments, we have evidenced that remote equatorial forcing can influence the northern part the Benguela Upwelling System as far as 24°S.

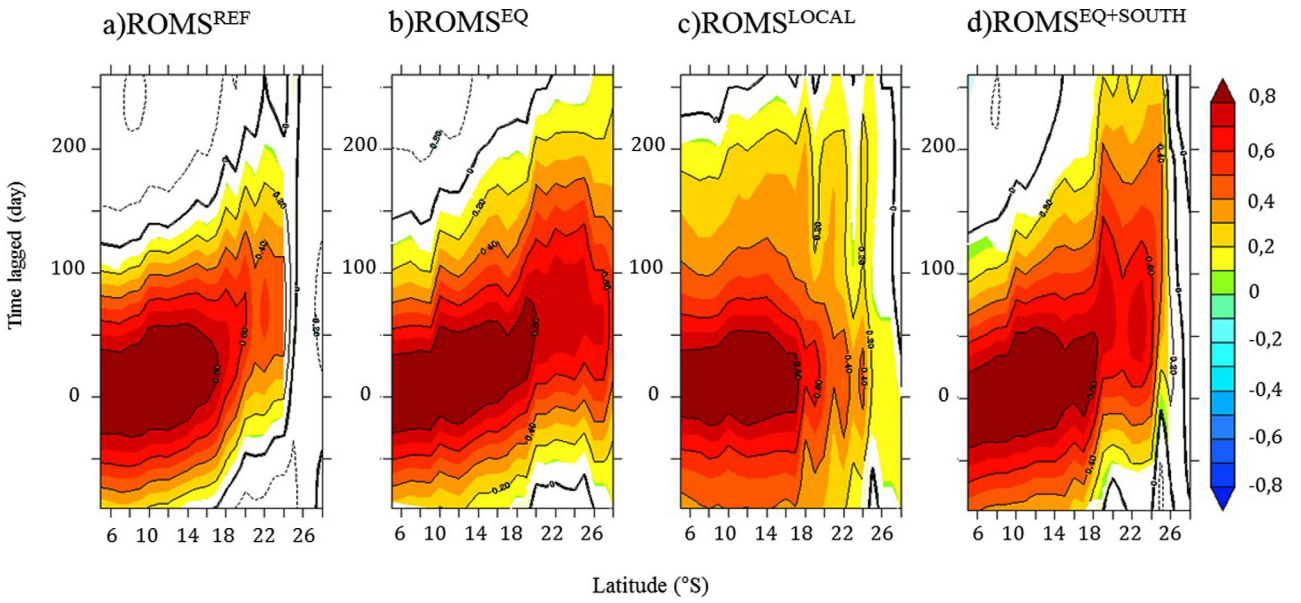

Figure 6. Lagged correlation between the time-series associated with the principal component of the first EOF (cf. Figure 5) of interannual alongshore density variability (IA) taken at 8°S and at each latitude along the southwest coast of Africa every 1°. Figures 6a–6d present the results of the four simulations: ROMS^{REF}, ROMS^{EQ}, ROMS^{LOCAL}, and ROMS$^{EQ+SOUTH}$, respectively. Contour lines are drawn every 0.2. The white color denotes negative or nonsignificant correlations (at 95% confidence level).

4.3. Most Southward Latitude of Poleward Propagation

Interestingly, Figure 6b illustrates CTW propagating further poleward in ROMS^{EQ}, when climatological surface and southern boundary forcing are prescribed, than in the most realistic simulation (ROMS^{REF}). Indeed, analysis of the most poleward latitude at which significant correlation can be detected (Figures 6a and 6b) shows that without disturbances CTW could impact vertical stratification up to the southern boundary of our domain at 30°S. Hence, this section is devoted to investigating the impact of different forcing that can modulate the most poleward latitude at which CTW signature can be observed.

First, the role of variability prescribed at the model's southern boundary is investigated using EOF analysis results of interannual density fluctuations (IA) for two sensitivity experiments, ROMS^{EQ} and ROMS$^{EQ+SOUTH}$ (Figures 6b and 6d). ROMS^{EQ} and ROMS$^{EQ+SOUTH}$ are paired experiments that differ only by the OBC at the southern boundary of our ROMS domain (cf. Table 1 and section 3.2), which are climatological (ROMS^{EQ}) or interannual (ROMS$^{EQ+SOUTH}$). As described previously, in ROMS^{EQ} (Figure 6b) we observed clear poleward propagations of interannual CTW, with significant lagged correlation all along the African southwest coast, as far as the Southern tip of the African continent. In comparison, ROMS$^{EQ+SOUTH}$ (Figure 6d) shows similar poleward CTW propagation with comparable phase speed (0.87 m.s^{-1}), but the 95% level significance in the PCs lagged correlation analysis does not extent as far southward, reaching only ~26°S. This result reveals that the interannual variability at 30°S can impact CTW propagation along the African coast. It is most likely that it is the interannual water transports of the energetic northward Benguela Current at 30°S, fed by the Agulhas Current and the South Atlantic Current [*Shannon*, 1985; *Gordon et al*., 1992], that modulates the ocean dynamics. Its signature and the associated mesoscale features [*Lutjeharms and van Ballegooyen*, 1988; *Duncombe Rae*, 1991] dominate the signal observed at interannual timescales in surface and subsurface from 30°S to 26°S and consequently constrains the most poleward latitude at which poleward CTW can be detected.

The interannual variability at the southern boundary (30°S) does not entirely explain the differences between the most southward latitude at which poleward CTW propagation can be detected in ROMS$^{EQ+SOUTH}$ (26°S) and in ROMS^{REF} (24°S). Given that the interannual variability of ROMS$^{EQ+SOUTH}$ is essentially influenced by two distinct forcing (the remote equatorial forcing and the southern boundary variability), while in ROMS^{REF} three forcing (equatorially remote, southern boundary, and local atmospheric variability) are at work, the local atmospheric forcing can also drive the ocean dynamics at interannual frequencies and limit CTW propagation. Thus, even if local atmospheric forcing is not dominant at interannual timescales,

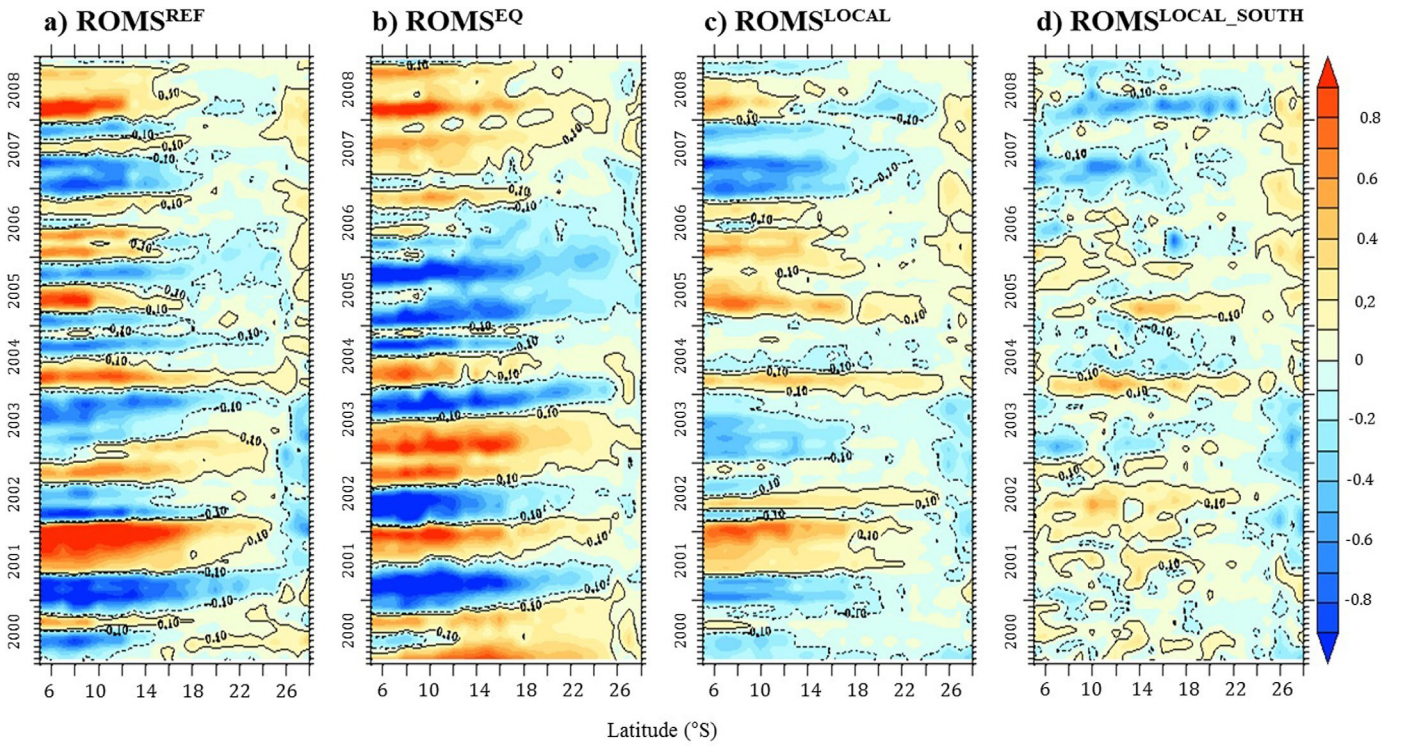

Figure 7. Space time diagram along the southwest coast of Africa of the interannual alongshore density time-series (IA) associated with the first EOF (cf. Figure 5). Figures 7a–7d present the results of the four simulations: ROMS^{REF}, ROMS^{EQ}, ROMS^{LOCAL}, and ROMS^{LOCAL_SOUTH}, respectively. Unit is kg.m^{-3}.

the nearshore wind stress variability can also enhance or compensate downwelling/upwelling associated with remotely forced CTW. This is illustrated in Figure 7 which displays the latitude-time diagram of the PCs of interannual along-shore density (IA) for the ROMS^{REF}, ROMS^{EQ}, ROMS^{LOCAL}, and ROMS^{LOCAL_SOUTH} simulations, respectively. Here, we remind the reader that in order to be able to compare PCs from one latitude to another, EOF spatial patterns have been normalized such as the maximum density anomalies are equal to 1 (cf. section 2.3).In agreement with our results, continuous coherent pattern portraying clear poleward propagation can be detected for the simulations including equatorially remote forcing (ROMS^{REF} and ROMS^{EQ}), with poleward CTW propagating more south in ROMS^{EQ}. Strong events, such as the 2000/2001 warm event or the 2003 cold event, propagate up to ~24°S (~30°S) in ROMS^{REF} (ROMS^{EQ}). When compared to ROMS^{REF} (Figure 7a) and ROMS^{EQ} (Figure 7b), ROMS^{LOCAL} (Figure 7c) shows higher frequency variability and counts a smaller number of major interannual events, either stationary or propagative (both poleward and equatorward). In addition, the signature of equatorial remote forcing and impact of local atmospheric forcing on the interannual density fluctuations can be in phase or out of phase to one another during some peculiar events and they can almost be visually added up to reconstitute the signal of ROMS^{REF}. As an example, during the year 2001, the two contributions (remote and local) were in phase, while in 2005 they were out of phase. In summary, evaluation of subsurface distribution of density and currents at interannual timescales reveals that local forcing generates subsequent interannual density variability. These anomalies could contribute to the intensification or weakening of coastal propagation signatures triggered by EKW. Thus, model experimentation shows that in addition to the southern boundaries entrances, local atmospheric forcing in the South-East Atlantic also modulates the most southward latitude at which remotely forced CTW propagation along the southwest coast of Africa can be detected.

It is worth noting that various mechanisms can trigger interannual variability in ROMS^{LOCAL} experiment. On the one hand, as well as internal model variability, wind-driven coastal upwelling or downwelling events, along with locally forced CTW [*Battisti and Hickey*, 1984; *Brink*, 1991] can be generated along the southwest coast of Africa. On the other hand, due to the design of our model configuration, interannual wind-stress variations in the eastern equatorial band (from 10°W to the African coast) can also force EKW, which in turn can trigger poleward CTW (cf. section 3.2). This contribution is now investigated using outputs of two

sensitivity experiments: ROMS^{LOCAL} and ROMS^{LOCAL_SOUTH} (cf. Table 1 and section 3.2), which differ only by the atmospheric forcing prescribed north of 4°S and set to either climatological (ROMS^{LOCAL_SOUTH}) or interannual conditions (ROM^{LOCAL}). Interannual subsurface density variations in ROMS^{LOCAL_SOUTH} (Figure 7d) are similar to those in ROMS^{LOCAL} (Figure 7c) and have, in particular, fewer interannual events than in ROMS^{REF} (Figure 7a) or ROMS^{EQ} (Figure 7b). In ROMS^{LOCAL_SOUTH}, the interannual wind-stress fluctuations force positive and negative interannual density events (2004, 2005, 2007, and 2008). Most of these events are also present in the ROMS^{LOCAL}. However, it is interesting to note that other events in ROMS^{LOCAL} (e.g., the 2001 warm event; Figure 7c) have no signature in ROMS^{LOCAL_SOUTH} (Figure 7d). Thus, they are not induced by local wind stress variations along the southwest coast of Africa but rather, they result from CTW propagation associated with EKW forced in the eastern equatorial Atlantic. Using a wavelet analysis of the subsurface interannual density field averaged between the MLD and 200 m depth, from 1°S to 24°S, within the 1° width coastal band, we quantified that the contribution of EKW forced in ROMS^{LOCAL} triggers 20% of the ROMS^{REF} interannual density variability (380–520 days). Similarly, the contribution of local atmospheric forcing along the western coast of Africa (simulated in ROMS^{LOCAL_SOUTH}) has been estimated to 9% of the ROMS^{REF} density variability. Thus, albeit being nonnegligible, these contributions remain largely lower than that of remote equatorial forcing, which explains 93% of the ROMS^{REF} coastal interannual density variability.

In summary, the investigation of the subsurface interannual density variability in the light of model experimentation confirms that remote equatorial forcing via CTW propagation is the main driving process of interannual variability along the southwest coast of Africa. These remotely forced CTW can propagate along the African southwest coast as far as 30°S, i.e., to the southern boundary of our model. However, the most poleward latitude at which they can be observed is modulated by the interannual variability at 30°S, as well as the interannual fluctuations of coastal wind forcing along the south-west African continent. While the impact of local forcing at interannual timescales along the coast is rather weak, the wind-forced CTW in the eastern equatorial part of the Atlantic basin are associated with subsequent upwelling/downwelling propagation events along the southwest coast. These locally wind-forced events can trigger significant interannual variability, which can overshadow the signature of the remotely forced CTW. Because remotely forced CTW explain most of the interannual variability, in the next section we further investigate their characteristics and described their impact in the Benguela Upwelling System during two major events: the downwelling event in 2001 and the upwelling event in 2003.

5. CTW Signature on Coastal Temperature, Currents, and Heat Budget: Results and Discussion

5.1. CTW Influence on Interannual Currents and Temperature

In this section, we discuss the mechanisms associated with the passage of a CTW using the ROMS^{EQ} simulation. The dynamical oceanic response to CTW propagation is first illustrated by showing cross-shore sections of simulated temperature and currents averaged between 1°S and 25°S during two major events: the 2001 downwelling event (Figure 8b) and the 2003 upwelling event (Figure 8c). Associated monthly climatology and interannual anomalies (IA) are also represented (see Figures 8d and 8e). Cross-shore sections were depicted at the mature phase of each event, defined as the maximum of SLIA and identified in Figure 8a as red and blue circles.

The downwelling event (from January to May 2001) is characterized by an increased poleward alongshore current from the surface down to a depth of 200 m (Figure 8f), compared to the climatological situation (Figure 8d), implying a reduction of the equatorward current in the surface layer (0–40 m depth: ~ -0.06 m.s^{-1}) and a strengthening of the poleward undercurrent in the subsurface layer (120–200 m; $\sim +0.04$ m.s^{-1}). In addition, a decrease of upward vertical currents can be observed within the 150 km coastal band, with a maximum value along the continental shelf. This significant reduction in coastal upwelling is associated with a decrease of the cross-shore current that is superimposed on the mean offshore Ekman transport, observed in the surface and subsurface. It also results in a nearshore deepening of the thermocline in the first 200 km from the coast and in the development of positive temperature anomalies down to a 140 m depth with a maximum value ($+1.8$°C) in the subsurface layer ($\sim$30 m depth; Figure 8f).

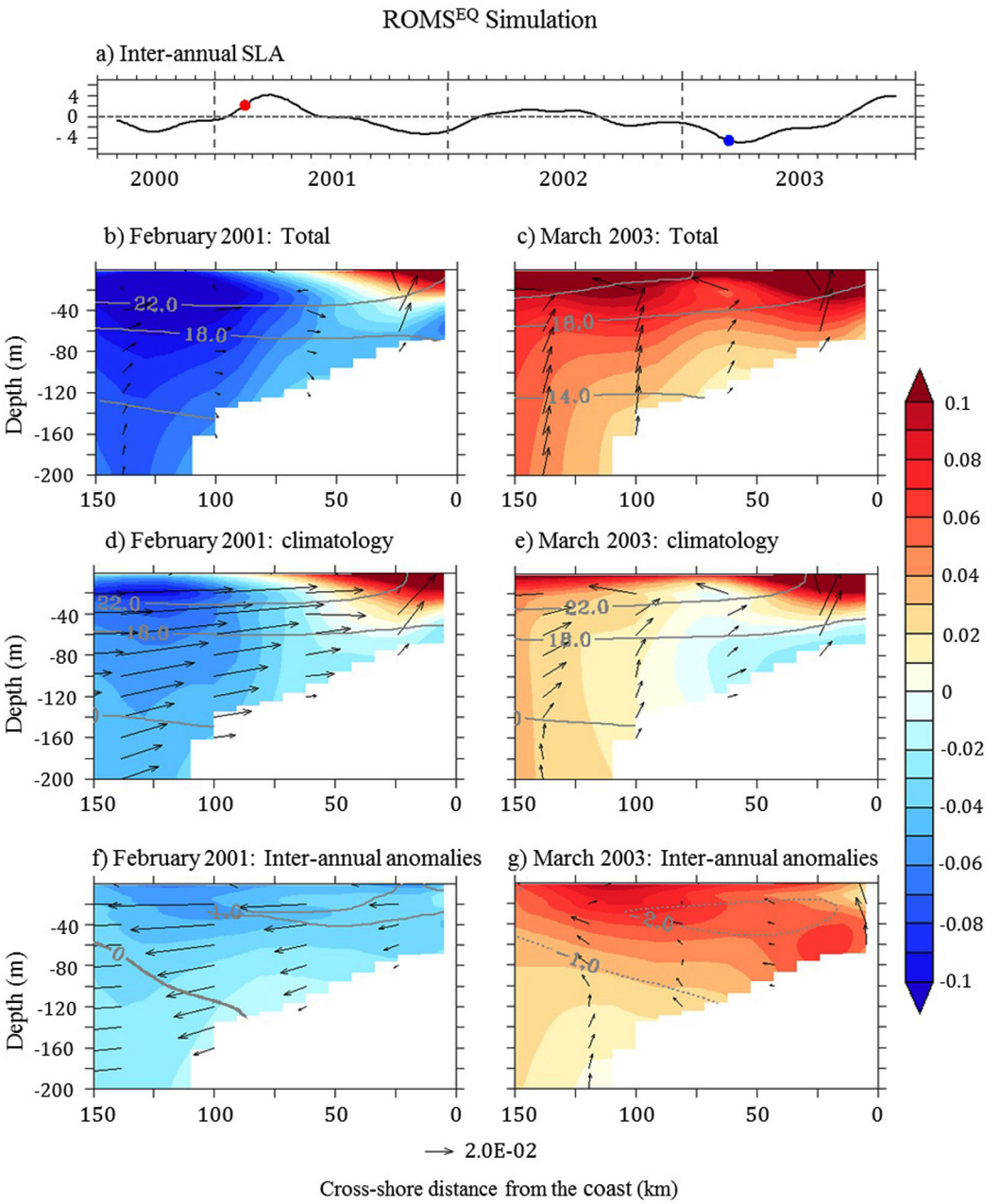

Figure 8. (a) Time-series of ROMS^{EQ} interannual SLA (full line, in cm), averaged over a 0.5°-width coastal band and between 1°S and 25°S. The red (blue) circle localizes the mature phase of the 2001 (2003) downwelling (upwelling) event. Vertical structures of total (b, c), climatological (d, e) and Interannual Anomalies (IA; f, g) of temperature (contour; °C), alongshore currents (color shading; m.s,$^{-1}$), cross-shore (arrows; m.s,$^{-1}$) and vertical currents (arrows; 2000 × m.s^{-1}) for the ROMS^{EQ} simulation, averaged between 1°S and 25°S. Left (right)-side plots correspond to the ocean dynamics during the mature phase of the downwelling (upwelling) event. To facilitate the visualization, vertical currents have been multiplied by 2000.

For the upwelling event (from June to August 2003) the situation is reversed, showing a strengthening of the upwelling dynamics with, in particular, an increase of the equatorward and upward vertical current in the top 200 m (Figures 8c, 8e, and 8g). Cross-shore current anomalies are weak, showing a slight decrease of shoreward currents in the subsurface layer and an increase of the shoreward current in the surface layer. The total circulation associated with the upwelling CTW passage contributes to a stronger upwelling of cold deep water in the first 200 km along the coast and to the development of negative temperature anomalies as deep as 280 m with a maximum value (∼−2.6°C) in the subsurface layer (30–40 m).

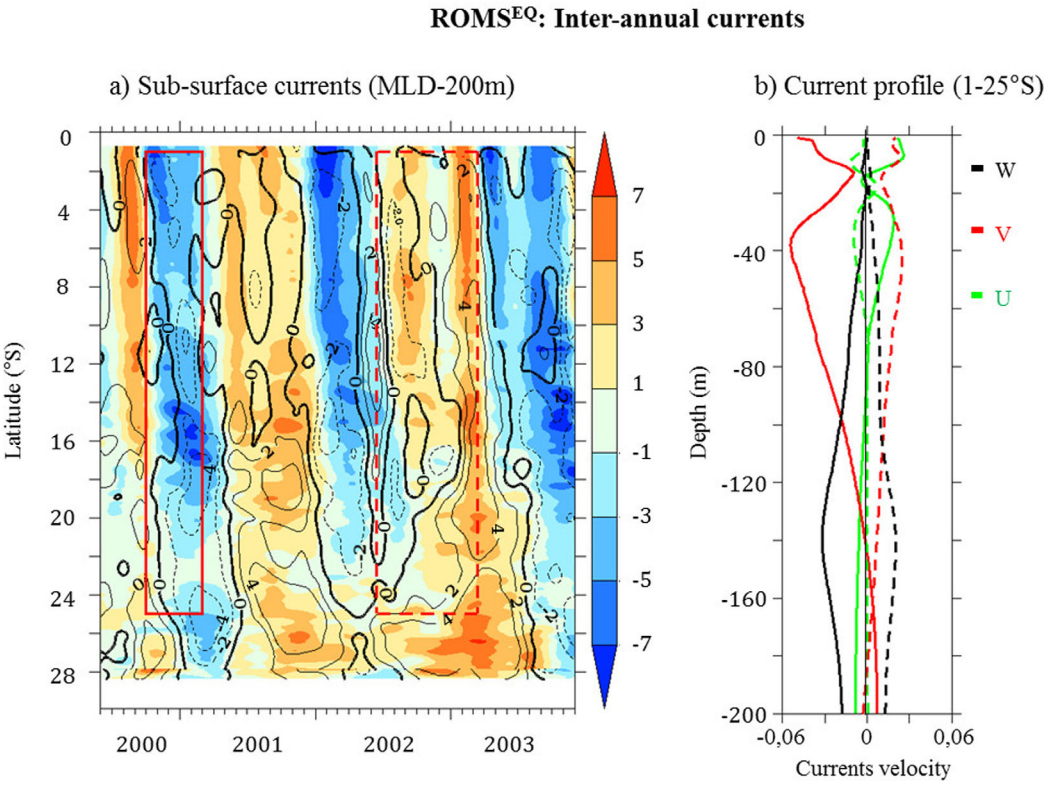

Figure 9. Interannual (IA) currents for ROMS^{EQ} simulation. (a) Time-latitude diagram of the vertical (m.d^{-1}; color shading) and the alongshore (20 × m.s^{-1}; black contour) currents which have been averaged over a coastal 1° width band and between the mixed layer depth and 200 meter depth. Red full and dashed boxes encircle the onset period of a downwelling (2001) and an upwelling (2003) event, respectively. (b) Full and dashed lines portray the vertical profile of the vertical (W; black lines; 100 × m.d^{-1}), the alongshore (V; red lines; m.s^{-1}) and the cross-shore (U; green lines; m.s^{-1}) currents averaged over the onset period of the 2001 downwelling event and the 2003 upwelling event, respectively. Vertical profiles have been averaged over a of 1° width coastal band and between 1°S and 25°S.

Thus, poleward propagation of downwelling/upwelling interannual CTW strongly influences alongshore and vertical current variability and induces a net nearshore temperature variation mostly in the subsurface. These results are summarized in Figure 9. In addition, Figure 9a shows that the signature of the CTW on coastal vertical and alongshore current interannual anomalies (IA) is continuous and extends from the equator up to 27°S. Note that either for a downwelling or an upwelling event, interannual modeled cross-shore currents are highly variable in space (from one latitude to another) and time (for the duration of the event). Two processes may explain this variability: Rossby Waves and westward propagating mesoscale eddies. The influence of CTW on the eddy activity in the eastern boundary regions has been investigated in *Zamudio et al*. [2001, 2006, 2007] for the North-East Pacific (12°N–24°N) and *Melsom et al*. [1999] for the Gulf of Alaska (46°N–60°N). They showed that a downwelling CTW can generate and/or strengthen anticyclonic eddies by accelerating the dominant poleward surface currents in these regions. Indeed, the reinforced jet is associated with stronger vertical and horizontal shears, which favor the development of baroclinic and barotropic instabilities. This is coherent with our results highlighting an increased variability of the poleward Angola undercurrent associated with interannual CTW propagations (Figures 8f and 8g). Accordingly, we observe that the mean coastal (200 km width band) EKE in ROMS^{EQ} is increased (decreased) by 70% (35%) during the onset of the 2001 (2003) event up to 20°S as compared with the ROMS^{CLIM} experiment. Over the 2000–2008 period, the mean EKE averaged over a 1.5° width coastal band between 10°S and 20°S is increased in ROMS^{EQ} by 53% as compared with ROMS^{CLIM}. This may be triggered by nonlinear effects associated with the dissymmetry of the CTW imprint on interannual coastal variability, showing more energetic warm events and longer and weaker cold events (cf. Figure 6). As an illustration, the skewness of the coastal SLIA averaged over 1° width coastal band and between 10°S and 20°S has been estimated to 0.29. But as pointed out by *Belmadani et al*. [2012], the increased EKE associated with equatorial remote forcing cannot be simply related to baroclinic instabilities and may rather be explained by changes in Rossby Wave activity and

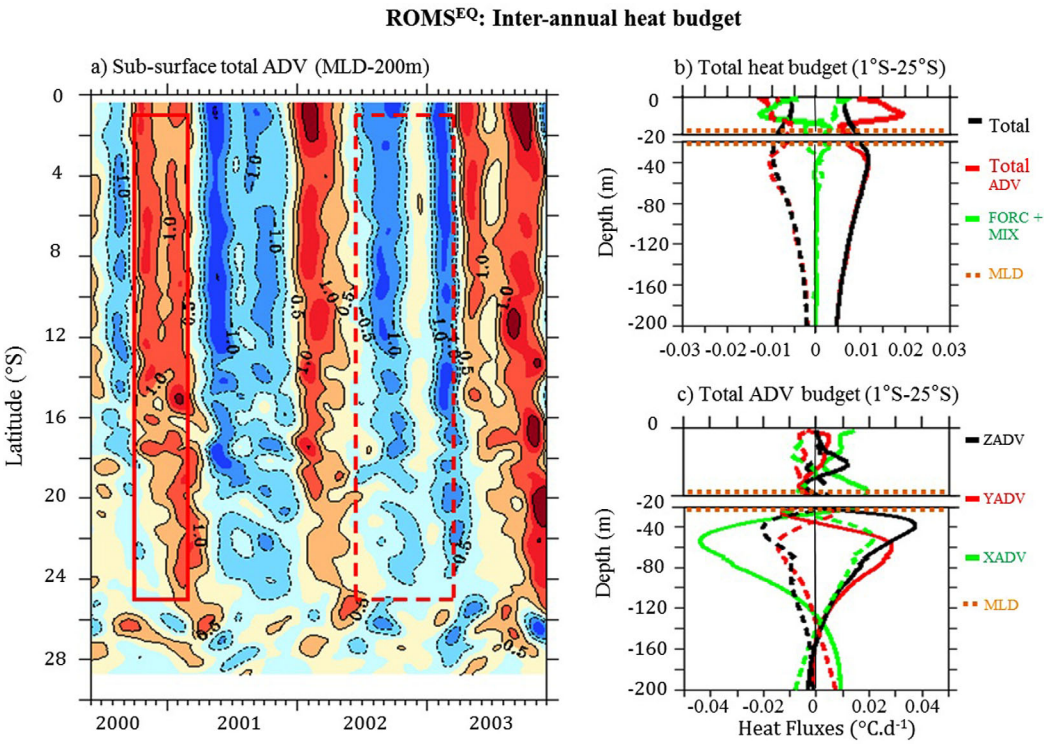

Figure 10. Heat budget of the ROMS^{EQ} simulation. (a) Time-latitude diagram of the summed up contribution of the Interannual (IA) temperature advection terms (zonal (XADV) + meridional (YADV) + vertical (ZADV)). All the advection terms have been averaged over a 1° width coastal band and between the Mixed Layer Depth (MLD) and 200 m depth. Red full and dashed boxes encircle the onset period of a downwelling (2001) and an upwelling (2003) event, respectively. (b) Vertical profiles of the IA total rate of change (Total; black lines), total advection (Total ADV; red lines), and the sum of the mixing and forcing terms (MIX+FORC; green lines). (c) Vertical profile of the IA zonal (XADV; red lines), meridional (XADV; black lines), and vertical (ZADV; green lines) temperature advection terms. Vertical profiles have been averaged over a 1° width coastal band and between 1°S and 25°S. Full (dashed) lines correspond to the downwelling (upwelling) event encircled by full (dashed) contours on Figure 10a. In Figures 10b and 10c, the orange-dashed line corresponds to the MLD. Unit is 0.01°C.d^{-1}.

by the surface alongshore current fluctuations. In conclusion, it is advisable to place a caveat on our interpretation of the cross-shore variability associated with CTW propagations.

5.2. Heat Budget

The analysis of the CTW signature on temperature and currents anomalies calls for further investigation of processes associated with the heat budget along the southwest coast of Africa. To do so, the processes responsible for temperature fluctuations are computed online to guarantee closure of the heat budget. Interannual Anomalies (IA) of the heat budget terms are then extracted offline. To be consistent with Figure 9, the budget tendency terms are averaged over the onset period of each event: the downwelling (2001) and upwelling (2003) events. Then, tendencies are averaged within the 1° width coastal band, which corresponds to the maximum signature of the CTW on the subsurface temperature (Figures 8f and 8g). As a first step, we examine the vertical profiles of interannual anomalies of different contributions to the heat budget balance averaged between 1°S and 25°S (Figure 10b). In agreement with Figure 8, the total rate of temperature change (TOTAL) is maximal in the subsurface below the Mixed Layer (ML), between 20 and 60 m depth, with a heat gain/loss of ~0.014°C.d^{-1}. Total advection (TOTAL ADV) is the main contributor to subsurface temperature anomalies, since the summed-up contribution of the advection terms represents 98% of the total rate of temperature change between a 20 and 60 m depth. It induces a continuous heat supply along the coast from the equator to 26°S, with an average value of 0.01°C.d^{-1} (Figure 10a). In contrast, within the ML, TOTAL ADV, and the combined contribution of vertical mixing and forcing terms (FORC) tend to compensate each other as they are of the same order of magnitude with opposite signs (for both events). In addition, it is interesting to note that most of the total surface variability within the ML is triggered by the surface forcing term (not shown), whose contribution tends to damp the ML interannual temperature anomalies. It is driven by coupling between ML depth and heat exchanges at the ocean-atmosphere

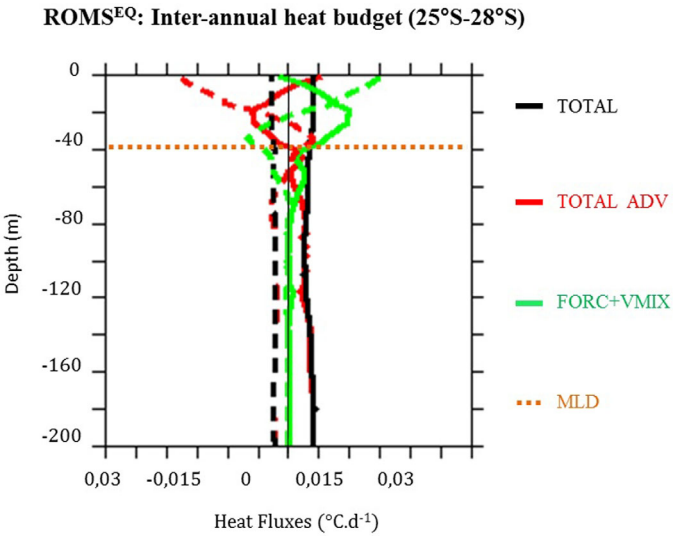

Figure 11. Same as Figure 10b. But for the 25°S–28°S averaged meridional band.

interface which is controlled by increased (decreased) SST associated with the passage of downwelling (upwelling) CTW. Furthermore, we estimated a lag between TOTAL ADV and FORC terms averaged within the ML of ∼1 month, with the TOTAL ADV term leading. This suggests that, for either a downwelling or an upwelling event, processes driving the interannual temperature variability in the surface and subsurface layers remain controlled by the advection terms, but in the ML ocean/atmosphere interactions damp the CTW signature on the SST. However, the damping associated with net heat flux contribution is most likely overestimated in ROMS^{EQ}, because of the use of climatological surface atmospheric fields in the bulk formulae (wind speed, temperature at 2 m, and humidity at 2 m). In order to quantify the ocean-atmosphere coupled response associated with the passage of CTW, it would be required to run ocean-atmosphere simulations in a coupled context, which is beyond the scope of this study.

Surprisingly, we have shown in Figures 6b and 9 that in ROMS^{EQ} (see Table 1 and section 3.2) for which atmospheric forcing and southern boundary oceanic conditions are climatological, remotely forced CTW can propagate up to 30°S (i.e., the southern edge of our ROMS domain). However, compared with dynamical signals, the subsurface thermodynamical signature associated with the passage of a CTW fades away around 26°S (Figure 10a), which is the position of the largest, most perennial and intense upwelling cell—the Lüderitz cell. Indeed, the heat budget within the 25°S–28°S latitude range, for the onset period of the downwelling (upwelling) event (Figure 11) is completely different to that presented in Figure 10b. For both events (downwelling/upwelling), the total rate of temperature change (solid/dash black line) is significantly weaker than nearer the equator and has a barotropic signature. TOTAL ADV (solid/dash red line) and MIX+FORC (solid/dash green line) terms have opposite signs and mostly compensate each other, but with a predominance of the MIX+FORC term. Both terms are maximum in the ML. Below the ML, the MIX+FORC term is almost zero and TOTAL ADV becomes dominant but with a small contribution. In addition, between 25°S and 28°S, the MLD is also more than twice as deep (∼40 m depth) than between 0°S and 25°S (Figure 10b). It is most likely that homogenization of water masses is associated with upwelling dynamics and turbulent mixing which reduce advection processes and heat supply/loss in the subsurface, where CTW signature in temperature is usually maximal. Even if CTW propagate along the coast up to 30°S, their signature in temperature is damped south of 26°S by the abrupt change in stratification associated with the Lüderitz upwelling cell. This result emphasizes the fundamental role of the mean state (i.e., stratification) for controlling the efficiency by which CTW can trigger temperature anomalies along the southwest coast of Africa through advection processes.

It is now worth examining the contribution of each of the advection terms on Interannual (IA) heat budget. Like Figures 10b and 10c also shows the vertical profiles for contributions of each temperature advection term: the zonal (east-west) advection (XADV-green line), the meridional (north-south) advection (YADV-red line), and the vertical advection (ZADV-black line). Results show that during both events (downwelling and upwelling), interannual temperature variations are mainly explained by contributions of the ZADV and YADV advection terms. These contributions are maximum below ML ($\sim\pm3.10^{-2}$°C.d^{-1} and $\pm2.4.10^{-2}$°C.d^{-1}, respectively) at the exact location of maximum total vertical currents and poleward undercurrent, respectively. In agreement with interannual currents variability (Figures 8a and 8b), during a downwelling/upwelling event, heat gain/loss associated with vertical advection is due to the reduction/increase of

upward vertical velocities (between 40 and 200 m depth) and therefore the reduction/increase of vertical transport of cold deep water at the coast. Now considering meridional advection, the increase/decrease in the alongshore poleward undercurrent induces a stronger/lower southward transport of equatorial warm waters and thus, contributes also to a heat modulation. The zonal advection term (XADV) is also maximum in subsurface and its contribution is the opposite of ZADV and YADV ($\sim\pm0.03°C.d^{-1}$). However, for cross-shore velocity, XADV contribution to the heat budget is highly variable in space and time. Thus, we cannot make conclusions for the XADV impact on interannual temperature variability along the African southwest coast.

In summary, for both downwelling and upwelling events, the sum of vertical and meridional advection terms mainly contributes to interannual temperature variability, while zonal advection (in subsurface) and forcing (in the ML) terms tend to balance the system. However, zonal advection by cross-shore currents is highly variable from one latitude to another; we must remain cautious about our conclusions regarding XADV contribution on interannual temperature variability. In addition, and contrary to our observations regarding oceanic dynamics (density and currents), the thermodynamical signature of CTW declines poleward of 26°S in the Lüderitz upwelling cell. This is due to the mean stratification associated with upwelling dynamics which reduces the efficiency of vertical advection.

6. Conclusion and Perspectives

In this paper, we have investigated the remote equatorial connection to oceanic variability along the southwestern African coast as far as the Benguela Upwelling System. Our approach is based on numerical experimentation with a high-resolution regional ocean model over the 2000–2008 period. First, the model was validated with available observed data set (in situ and satellite observations). The model reproduces realistically the mean state in the South-East Atlantic Ocean (including a realistic MLD, and coastal upwelling) and interannual variability (of SLA and temperature) compared to observed data. Model has been shown to be skillful in reproducing EKW propagations along the equator and CTW propagations along the Southwestern African coast.

Given that the model is able to simulate a realistic mean state and interannual variability, a sensitivity analysis with a set of six numerical experiments was designed to quantify the relative contribution of remote equatorial forcing (associated with EKW) and local atmospheric forcing (momentum and heat fluxes) in the South-East Atlantic Ocean. These experiments differ only by their open boundary conditions or the local atmospheric forcing being either climatological or total. In agreement with previous studies, analysis of SLA indicates that interannual (380–520 days) oceanic variability in the equatorial Atlantic and along the African coast are primarily explained by remote equatorial forcing [i.e., *Lübbecke et al.*, 2010], while subseasonal variability is controlled by local forcing [*Goubanova et al.*, 2013]. Thanks to this sensitivity analysis, we quantified for the first time that at interannual timescales, remote forcing contributes to 89% of coastal SLA variability, compared to 29% for local forcing, along the southwest coast of Africa for the 2000–2008 period.

As equatorial forcing is the main forcing for interannual variability in the South-East Atlantic Ocean, CTW characteristics are then evaluated. Analyses of interannual SLA reveal poleward propagations of CTW triggered by EKW up to 17°S, just north of the Benguela Upwelling System. As expected, baroclinic CTW have a strong signature in the subsurface, and this allowed us to detect poleward propagative CTW signature on interannual subsurface density and current anomalies over the first 200 m depth along the African southwest coast. It highlights that without disturbances, CTW can propagate poleward up to 30°S (the southern edge of our model). However, their amplitude and the most poleward latitude at which they can be detected is modulated by (1) the interannual variability of OBC at 30°S associated with the equatorward Benguela current, and (2) the coastal interannual wind forced CTW and upwelling dynamics. The mean CTW phase speed estimated using SLIA and subsurface density and current analyses was estimated to 1.09 and $\sim$0.89 $m.s^{-1}$, respectively, suggesting the propagation of a third baroclinic mode CTW. We have shown that CTW can affect the oceanic circulation in the BUS and modulate temperature structure (and, by implication, the biogeochemical dynamics).

Overall, our study also illustrates CTW impact on interannual temperature variability with temperature anomalies up to $\pm$2°C located between the base of MLD and 200 m depth within a 200 km cross-shore band from the coast. In the model sensitivity experiment, in which the sole interannual forcing prescribed is

that of remote equatorial forcing ($ROMS^{EQ}$, with climatological surface and southern boundary forcing), CTW imprint on the temperature field is detectable from the equator up to 26°S, while we find evidence of CTW signature on currents and density as far as 30°S. Therefore, in order to investigate the mechanisms controlling interannual coastal temperature variability associated with CTW events, the different contributions to temperature changes were analyzed. First, we highlight that the maximum of temperature variability, located below the MLD in subsurface, is due to advection processes which are balanced in the surface by the ocean-atmosphere forcing term. In the subsurface layer, advection processes represent 98% of the total rate of temperature change and induce a continuous heat supply/decrease from the equator up to 26°S with a mean value of $\pm$0.3°C.month^{-1} during a downwelling/upwelling event. Indeed, vertical and meridional advection terms contribute to temperature change through modulation of poleward alongshore and vertical currents. In the surface layer, ocean/atmosphere coupling tends to damp the interannual temperature variability and consequently, CTW impact on SST is not detectable. South of 26°S, in both the surface and subsurface layers, thermodynamical signature of CTW is also damped due to the change in stratification associated with the intense Lüderitz upwelling cell.

This study highlights the dominant role of equatorial forcing on interannual dynamics and thermodynamics of the coastal South-East Atlantic Ocean over the 2000–2008 period. This is especially true in the subsurface, up to the northern part of the Benguela Upwelling System. In this context, CTW are expected to significantly impact both the biogeochemical dynamics of the Benguela Upwelling System and marine ecosystem at interannual timescales. Thus, our future work will focus on analyses and quantification of CTW on key environmental parameters such as oxygen and nutrient concentrations, productivity, greenhouse, and toxic gas emissions in the Benguela Upwelling System.

Appendix A

In this appendix, we evaluate the realism of the mean state and interannual variability simulated in $ROMS^{REF}$, which is our most realistic experiment. This experiment provides a benchmark for evaluating sensitivity experiments to surface forcing and open boundary conditions for investigation of interannual variability in the South-East Atlantic Ocean.

A1. Observed Data Sets for Validation

Climatology, satellite and in situ data are used to evaluate the performance of the $ROMS^{REF}$ simulation in this study.

A1.1. Climatology

A1.1.1. CSIRO Atlas of Regional Seas 2009

We use monthly temperature, salinity, density, and mixed layer depth climatologies of the 2009 CSIRO Atlas of Regional Seas (CARS2009) available at www.cmar.csiro.au/cars. CARS2009 data cover the global ocean on a 0.5° $\times$ 0.5° horizontal grid with 79 vertical levels. It combines all available oceanic data over the last 50 years using rigorous quality controls and an adaptive-length-scale loess mapper to maximize resolution in data-rich regions. More details on input data sources and method can be found in *Ridgway et al.* [2002] and *Dunn and Ridgway* [2002].

A1.2. Satellite Data

A1.2.1. SST

Sea Surface Temperature (SST) is derived from the Tropical Rainfall Measuring Mission (TRMM) [*Kummerow et al.* [2000] Microwave Imager (TMI). We use daily optimally interpolated (TMI-OI) SST product over the 2000–2008 period with a resolution of 0.25° $\times$ 0.25°, provided by Remote Sensing Systems (www.remss.com). In TMI-OI SST, aliasing by the diurnal cycle due to sun-asynchronous orbit of TRMM satellite is corrected by a simple empirical model of diurnal warming [*Gentemann et al.*, 2003] and an extensive land-mask is applied to remove land contamination [*Gentemann et al.*, 2010]. Despite these limitations, this data set has proven suitable for the study of coastal eastern boundary system dynamics (upwelling, CTW) in the Benguela [*Goubanova et al.*, 2013] and Humboldt [*Dewitte et al.*, 2011; *Illig et al.*, 2014] upwelling systems.

A1.2.2. In Situ Data From Cruises

Several in situ measurements for temperature and salinity were used to evaluate the performance of the $ROMS^{REF}$ simulation in the area under study. Data were collected during the M57/2 of R/V Alexander expedition in February 2003 [*Zabel et al.*, 2003; *Kuypers et al.*, 2005] and the AHAB1 of R/V Alexander von Humboldt in January 2004 [*Lavik et al.*, 2009] over the Namibian Upwelling System along sections at different latitudes

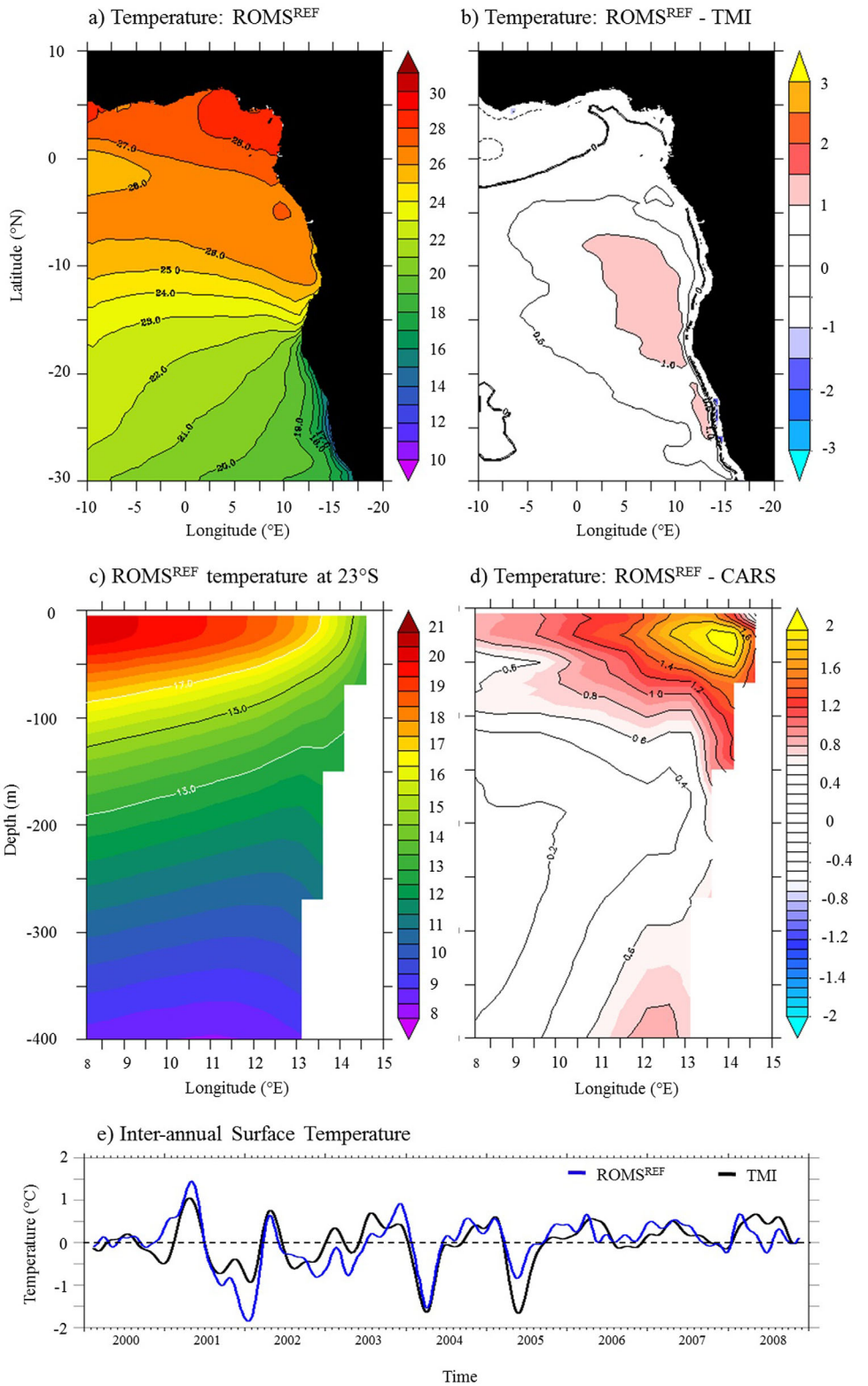

Figure A1. (a) Map of mean (2000–2008) Sea Surface Temperature (SST) of ROMS^{REF} simulation, and (b) differences between model and TMI SST. (c) ROMS^{REF} mean vertical temperature section at 23°S (2000–2008) as a function of depth (meters) and longitude (°E), and (d) differences between model and CARS2009. Black line stands for the mean position of the 15°C isotherm and the white lines correspond to the 17°C and 13°C isotherm, respectively. (e) Interannual SST Anomalies (IA) of ROMS^{REF} (blue) and TMI (black) averaged over Angola Benguela Area (10°S–20°S; 8°E–15°E). Unit is °C.

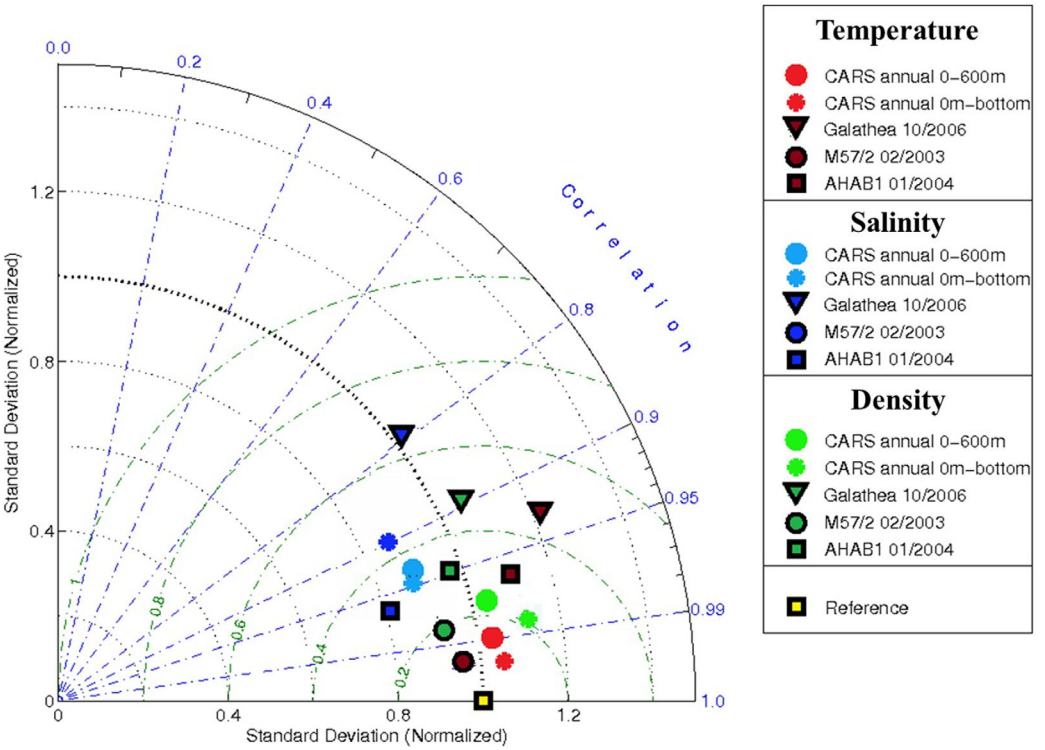

Figure A2. Taylor diagram for (first group in red) temperature, (second group in blue) salinity, and (third group in green) density: ROMS^{REF} simulation skills are estimated by comparison to data from CARS 2009, the METEOR expedition 57/2 in February 2003 (transects at 23°S, 24.4°S, and 25.5°S), the AHAB1 expedition in January 2004 (transects at 22°S, 23°S, 24°S, 25°S, 26.7°S), and the Galathea data in October 2006 (surface data, at five stations and Triaxus data). The radial distance from the origin is proportional to the standard deviation of a pattern (normalized by the standard deviation of the data). The green-dashed lines measure the distance from the reference point (yellow square) and indicate the RMS error. The correlation between both fields is given by the azimuthally position. Mean biases are given in Table A1. For the comparison with CARS2009 database, model outputs were averaged over the 2000–2008 period, while for the comparison with in situ data, 5 day averaged model outputs are picked at the closest date to the in situ measurements.

between 23°S and 27°S. The in situ data collected in October 2006, during the Danish Galathea expedition (courtesy of L. L. Soerensen, National Environmental Research Institute, Danemark) were also used [see *Gutknecht et al*., 2013, for details and in particular their Figure 3 for location of the different cruises].

A2. Model Skills

A2.1. Mean State (2000–2008)

The model mean state was estimated over the 2000–2008 period. First, the SST mean state was evaluated to check the heat fluxes equilibrium at the interface. The mean SST of the ROMS^{REF} simulation is displayed in Figure A1, along with the differences between mean SST of ROMS^{REF} and TMI satellite data (Figure A1b). In ROMS^{REF}, the signature of the Benguela upwelling is clearly marked within a 200 km wide coastal band from 19°S to 30°S, in agreement with observations and the literature [*Boyer et al*., 2000; *Shillington et al*., 2006]. Mean ROMS^{REF} SST is warmer than observations over the entire domain except in the Gulf of Guinea (Figure A1b). Maximum differences between ROMS^{REF} and TMI are ~1°C and are located in the Angola-Benguela Frontal Zone (ABFZ) and along the African coast between 24°S and 28°S. Although this may reflect a model deficiency, it is likely related to a shift of the Benguela-Angola front position (where the surface temperature gradient is maximum). We have estimated this shift to 1° southward. Despite these considerations, the model simulates a realistic mean SST, with a spatial correlation between model and observation above 0.99 and a mean bias lower than 0.6°C (not shown).

To further assess the realism of the subsurface vertical structure simulated in ROMS^{REF} simulation, Figure A1b displays the mean ROMS^{REF} cross-shore vertical structure of temperature at 23°S along with the differences between ROMS^{REF} and CARS2009 climatology. The signature of the coastal upwelling off Namibia can be depicted in the 15°C isotherm position that is tilted upward 6° of longitude from the coast, both in ROMS^{REF} and in the observations. Off-shore, the model is slightly warmer than the observations (between

Table A1. Mean Biases for Temperature (°C), Salinity, and Density (kg.m^{-3}) Between ROMS^{REF} Simulation and In Situ Data

	Temperature	Salinity	Density
CARS annual 0–600 m	0.5910	−0.0626	−0.1612
CARS annual 0–bottom	0.2788	−0.0130	−0.0930
M57/2 Feb 2003 23S	0.7979	−0.0054	−0.0782
M57/2 Feb 2003 24.4S	0.604	0.0386	−0.0224
M57/2 Feb 2003 25.5S	0.2428	0.0039	−0.0684
AHB1 Jan 2004 22S	0.7899	−0.0166	−0.2083
AHB1 Jan 2004 23S	0.5383	−0.0477	−0.2334
AHB1 Jan 2004 24S	0.2257	−0.0430	−0.2078
Galathea Oct 2006	0.1581	−0.0382	−0.1862
AHB1 Jan 2004 27S	0.7494	0.0470	−0.2234
AHB1 Jan 2004 26S	0.7432	0.0760	−0.1993
AHB1 Jan 2004 25S	0.4837	0.2084	−0.2585

0.1°C and 0.6°C). Along the coast, ROMS^{REF} temperature is warmer, with a maximum difference between model and observations of ∼2°C, localized in the subsurface within 50 km off the coast. The latter is associated with the SODA temperature field that exhibits similar bias (∼2.3°C, confined in the surface layer over 1° cross-shore distance from the coast) at the model southern open boundary (30°S) which is advected equator-ward along the coast over the continental shelf driven by the Benguela current (not shown). Nevertheless, despite this bias, the SODA reanalysis has been used in our simulations as in previous studies because it has shown good skill for the study of the equatorial Kelvin waves dynamics in the Pacific [*Dewitte et al*., 2008a,; *Illig et al*., 2014] and Atlantic Oceans [*Goubanova et al*., 2013].

To further evaluate the subsurface mean state, spatial statistics of the model mean temperature, salinity, and density fields (averaged over the 2000–2008 period) are estimated against CARS2009 data. They are summarized in the Taylor diagram [*Taylor*, 2001] presented in Figure A2. We averaged model solution and data over the whole water column, as well as in the upper 600 m depth. Spatial correlation, normalized standard deviation, and normalized centered RMS error (Figure A2), as well as mean bias (Table A1) between model and data are estimated over the ROMS domain extending from 10°W to the African coast and from 30°S to 7°N. The spatial correlation usually remains above 0.98 for temperature and density and around 0.93 for salinity. The normalized standard deviation is between 0.1 and 0.4 and the normalized centered pattern RMS error less than 1.1 for temperature, between 1 and 1.2 for density and around 0.9 for salinity. In Table A2, mean biases illustrate the overestimation of modeled temperature and salinity. In general, the largest temperature differences are located in the surface layer (0–100m, not shown). In this layer, simulated temperature is on average ∼1°C warmer. Salinity is overestimated at the mouth of rivers and in the Gulf of Guinea.

Despite some bias, ROMS^{REF} configuration is able to realistically simulate the mean state for temperature, salinity, and density in the South-East Atlantic Ocean. We further investigate the interannual variability, which is the main interest of the present study. We focus our analysis on the key parameters associated with model dynamics (temperature, density, and sea level).

A2.2. Interannual Variability

First, a model/data comparison for interannual variability is presented using the Taylor diagram (Figure A2) that compares temperature, salinity, and density profiles and sections between ROMS^{REF} and in situ data from M57/2 (February 2003), AHAB1 (January 2004), Galathea (October 2006) cruises at different periods and at different locations in the Benguela Upwelling System [see *Gutknecht et al*., 2013, for location and period of the different cruises]. Overall, our results are statistically fair with a spatial correlation coefficient ranging between 0.8 (salinity) and 0.97 (temperature and density), a normalized standard deviation between 0.9 and 1.1 and a normalized centered RMS difference between 0.2 and 0.4.

We turn our attention to the comparison between model and satellite observations (TMI) for Sea Surface Temperature Interannual Anomalies (SSTIA). Figure A1c shows SSTIA of the reference experiment ROMS^{REF} and TMI averaged over the Angola Benguela Area (ABA; 10°S–20°S/8°E–15°S). The ABA region shows a noticeable interannual signal with anomalies ranging from 1°C to 2°C, for observations as well as model simulation. The model is specifically good for the extreme event and captures most of the observed interannual SST variability (including the Benguela Niño of 2001 documented by *Rouault et al*. [2007]). However, interannual variability in the ABA is overestimated by the model. Correlations between SSTIA from the model and observations are 0.7.

Finally, Sea Level Interannual Anomalies (SLIA) are evaluated against AVISO data. Figure 3 shows the correlation coefficient between ROMS^{REF} and AVISO data. From 17°S to the southern boundary (30°S), the correlation is not significant (according to *p*-value statistical test—*Best and Roberts*, [1975]). This has to be

attributed to mesoscale activity: although mean mesoscale variability is well represented in the model (not shown), absence of data assimilation precludes the collocation of modeled and observed eddies (not shown). Therefore, in regions where mesoscale activity dominates the SLIA signal, the correlation between model and data is low. Elsewhere, agreement between model and observations is statistically significant, especially along the equatorial wave guide and along the southwest coast of Africa, with correlation values larger than 0.6 and RMS differences lower than 1 cm (not shown). This suggests the presence of linear propagative waves in the ROMS^{REF} simulation. Note that further analysis is presented in the paper (see sections 4.1 and 4.2) which outlines the good representation of modeled propagative waves in terms of period, phase speed, and amplitude as compared to satellite data.

In conclusion, interannual oceanic dynamics are well represented in the areas of interest for this study.

Acknowledgments

We would like to thank the Centre National d'Etudes Spatiales, France (CNES) for their financial support (OSTST–TOSCA project "EBUS-SOUTH"). Marie-Lou Bachèlery was supported by a PhD fellowship from the Centre National de la Recherche Scientifique (CNRS). Bruno Michon, funded by the Région Midi-Pyrénées is acknowledged for preliminary results of this work. We thank the research center and institutes for the development and the distribution of following data sets: CSIRO Marine and Atmospheric for CARS 2009 database, the Remote Sensing Systems, sponsored by the NASA Earth Science for TMI-OI data, the Centre de Recherche et d'Exploitation Satellitaire (CERSAT) for QuikSCAT data and the Texas A&M University for SODA reanalysis. We also thank the IOW scientists (V. Mohrholz and H. Lass) for sharing the Benguela Upwelling System in situ data of the 2003 and 2004 cruises, as well as the British Oceanographic Data Center (BODC) for the AMT data. The authors wish to acknowledge the use of the Ferret program (http://ferret.pmel.noaa.gov) for analysis and graphics in this paper. Ferret is a product of NOAA's Pacific Marine Environmental Laboratory. The model grid, forcing, and initial conditions were built using the ROMSTOOLS package [*Penven et al*., 2008]. We express our special thanks to Patrick Marchesiello (LEGOS, France) and Gildas Cambon (LPO, France) for advice and explanations on the ROMS model. This work was performed using HPC resources from CALMIP(grant 2013–2014—P1134).

References

Backeberg, B. C., P. Penven, and M. Rouault (2012), Impact of intensified Indian Ocean winds on mesoscale variability in the Agulhas system, *Nat. Clim. Change*, *2*(8), 608–612, doi:10.1038/nclimate1587.

Battisti, D. S., and B. M. Hickey (1984), Application of remote wind-forced coastal trapped wave theory to the Oregon and Washington coasts, *J. Phys. Oceanogr.*, *14*(5), 887–903, doi:10.1175/1520-0485.

Belmadani, A., V. Echevin, B. Dewitte, and F. Colas (2012), Equatorially forced intraseasonal propagations along the Peru-Chile coast and their relation with the nearshore eddy activity in 1992–2000: A modeling study, *J. Geophys. Res.*, *117*, C04025, doi:10.1029/2011JC007848.

Best, D. J., and D. E. Roberts (1975), Algorithm AS 89: The upper tail probabilities of Spearman's Rho, *J. R. Stat. Soc. Ser. C*, *24*(3), 377–379, doi:10.2307/2347111.

Boyer, D., J. Cole, and C. Bartholomae (2000), Southwestern Africa: Northern Benguela current region, *Mar. Pollut. Bull.*, *41*(1–6), 123–140, doi:10.1016/S0025-326X(00)00106-5.

Brink, K. H. (1982), A comparison of long coastal trapped wave theory with observations off Peru, *J. Phys. Oceanogr.*, *12*(8), 897–913, doi:10.1175/1520-0485.

Brink, K. H. (1991), Coastal-trapped waves and wind-driven currents over the continental shelf, *Annu. Rev. Fluid Mech.*, *23*(1), 389–412, doi:10.1146/annurev.fl.23.010191.002133.

Brink, K. H., J. S. Allen, and R. L. Smith (1978), A study of low-frequency fluctuations near the Peru Coast, *J. Phys. Oceanogr.*, *8*(6), 1025–1041, doi:10.1175/1520-0485.

Cane, M. A., and E. S. Sarachik (1979), Forced baroclinic ocean motions. 3. Linear equatorial basin case, *J. Mar. Res.*, *37*(2), 355–398.

Carr, M.-E. (2002), Estimation of potential productivity in eastern boundary currents using remote sensing, *Deep Sea Res., Part II*, *49*(1–3), 59–80, doi:10.1016/S0967-0645(01)00094-7.

Carr, M.-E., and E. J. Kearns (2003), Production regimes in four eastern boundary current systems, *Deep Sea Res., Part II*, *50*(22–26), 3199–3221, doi:10.1016/j.dsr2.2003.07.015.

Carton, J. A., and B. S. Giese (2008), A reanalysis of ocean climate using simple ocean data assimilation (SODA), *Mon. Weather Rev.*, *136*(8), 2999–3017, doi:10.1175/2007MWR1978.1.

Carton, J. A., G. Chepurin, X. Cao, and B. Giese (2000), A simple ocean data assimilation analysis of the global upper ocean 1950–95. Part I: Methodology, *J. Phys. Oceanogr.*, *30*(2), 294–309, doi:10.1175/1520-0485.

Carton, J. A., B. S. Giese, and S. A. Grodsky (2005), Sea level rise and the warming of the oceans in the Simple Ocean Data Assimilation (SODA) ocean reanalysis, *J. Geophys. Res.*, *110*, C09006, doi:10.1029/2004JC002817.

Chavez, F. P., and M. Messié (2009), A comparison of eastern boundary upwelling ecosystems, *Prog. Oceanogr.*, *83*(1–4), 80–96, doi:10.1016/j.pocean.2009.07.032.

Chelton, D. B., R. A. de Szoeke, and M. G. Schlax (1998), Geographical variability of the first baroclinic Rossby radius of deformation, *J. Phys. Oceanogr.*, *28*(3), 433–460.

Clarke, A. J. (1983), The reflection of equatorial waves from oceanic boundaries, *J. Phys. Oceanogr.*, *13*(7), 1193–1207, doi:10.1175/1520-0485.

Clarke, A. J., and R. Ahmed (1999), Dynamics of remotely forced intraseasonal oscillations off the western coast of South America, *J. Phys. Oceanogr.*, *29*(2), 240–258, doi:10.1175/1520-0485.

Colas, F., X. Capet, J. C. McWilliams, and A. Shchepetkin (2008), 1997–1998 El Niño off Peru: A numerical study, *Prog. Oceanogr.*, *79*(2), 138–155.

Cravatte, S., J. Picaut, and G. Eldin (2003), Second and first baroclinic Kelvin modes in the equatorial Pacific at intraseasonal timescales, *J. Geophys. Res.*, *108*(C8), 3266, doi:10.1029/2002JC001511.

Cury, P., and L. Shannon (2004), Regime shifts in upwelling ecosystems: Observed changes and possible mechanisms in the northern and southern Benguela, *Prog. Oceanogr.*, *60*(2–4), 223–243, doi:10.1016/j.pocean.2004.02.007.

Debreu, L., C. Vouland, and E. Blayo (2008), AGRIF: Adaptive grid refinement in Fortran, *Comput. Geosci.*, *34*(1), 8–13, doi:10.1016/j.cageo.2007.01.009.

Debreu, L., P. Marchesiello, P. Penven, and G. Cambon (2012), Two-way nesting in split-explicit ocean models: Algorithms, implementation and validation, *Ocean Modell.*, *49–50*, 1–21, doi:10.1016/j.ocemod.2012.03.003.

Delecluse, P., J. Servain, C. Levy, K. Arpe, and L. Bengtsson (1994), On the connection between the 1984 Atlantic Warm Event and the 1982–1983 Enso, *Tellus Ser. A*, *46*(4), 448–464, doi:10.1034/j.1600-0870.1994.t01-1-00009.x.

Dewitte, B., S. Purca, S. Illig, L. Renault, and B. S. Giese (2008a), Low-frequency modulation of intraseasonal equatorial Kelvin wave activity in the Pacific from SODA: 1958–2001, *J. Clim.*, *21*(22), 6060–6069, doi:10.1175/2008JCLI2277.1.

Dewitte, B., M. Ramos, V. Echevin, O. Pizarro, and Y. duPenhoat (2008b), Vertical structure variability in a seasonal simulation of a medium-resolution regional model of the Eastern South Pacific, *Prog. Oceanogr.*, *79*(2–4), 120–137, doi:10.1016/j.pocean.2008.10.014.

Dewitte, B., S. Illig, L. Renault, K. Goubanova, K. Takahashi, D. Gushchina, K. Mosquera, and S. Purca (2011), Modes of covariability between sea surface temperature and wind stress intraseasonal anomalies along the coast of Peru from satellite observations (2000-2008), *J. Geophys. Res.*, *116*, C04028, doi:10.1029/2010JC006495.

Dewitte, B., et al. (2012), Change in El Nino flavours over 1958–2008: Implications for the long-term trend of the upwelling off Peru, *Deep Sea Res., Part II*, *77–80*, 143–156, doi:10.1016/j.dsr2.2012.04.011.

Ducet, N., P. Y. Le Traon, and G. Reverdin (2000), Global high-resolution mapping of ocean circulation from TOPEX/Poseidon and ERS-1 and-2, *J. Geophys. Res.*, *105*(C8), 19,477–19,498, doi:10.1029/2000JC900063.
Duncombe Rae, C. M. (1991), Agulhas retroflection rings in the South Atlantic Ocean; an overview, *S. Afr. J. Mar. Sci.*, *11*, 327–344.
Dunn, J. R., and K. R. Ridgway (2002), Mapping ocean properties in regions of complex topography, *Deep Sea Res. Part I*, *49*(3), 591–604, doi:10.1016/S0967-0637(01)00069-3.
Echevin, V., F. Colas, A. Chaigneau, and P. Penven (2011), Sensitivity of the Northern Humboldt Current System nearshore modeled circulation to initial and boundary conditions, *J. Geophys. Res.*, *116*, C07002, doi:10.1029/2010JC006684.
Echevin, V., A. Albert, M. Lévy, M. Graco, O. Aumont, A. Piétri, and G. Garric (2014), Intraseasonal variability of nearshore productivity in the Northern Humboldt Current System: The role of coastal trapped waves, *Cont. Shelf Res.*, *73*, 14–30, doi:10.1016/j.csr.2013.11.015.
Fairall, C. W., E. F. Bradley, D. P. Rogers, J. B. Edson, and G. S. Young (1996), Bulk parameterization of air-sea fluxes for tropical ocean-global atmosphere coupled-ocean atmosphere response experiment, *J. Geophys. Res.*, *101*(C2), 3747–3764, doi:10.1029/95JC03205.
Field, J. G., and F.A. Shillington (2005), Variability of the Benguela current system, In *The Sea, vol. 14, The Global Coastal Ocean, Interdisciplinary Regional Studies And Syntheses*, edited by A. R. Robinson and K. H. Brink, pp. 833–860, Harvard Univ. Press, Cambridge, Mass.
Florenchie, P., J. R. E. Lutjeharms, C. J. C. Reason, S. Masson, and M. Rouault (2003), The source of Benguela Niños in the South Atlantic Ocean, *Geophys. Res. Lett.*, *30*(10), 1505, doi:10.1029/2003GL017172.
Florenchie, P., C. J. C. Reason, J. R. E. Lutjeharms, M. Rouault, C. Roy, and S. Masson (2004), Evolution of interannual warm and cold events in the Southeast Atlantic Ocean, *J. Clim.*, *17*(12), 2318–2334, doi:10.1175/1520-0442.
Fréon, P., M. Barange, and J. Arístegui (2009), Eastern boundary upwelling ecosystems: Integrative and comparative approaches, *Prog. Oceanogr.*, *83*(1–4), 1–14, doi:10.1016/j.pocean.2009.08.001.
Gentemann, C. L., C. J. Donlon, A. Stuart-Menteth, and F. J. Wentz (2003), Diurnal signals in satellite sea surface temperature measurements, *Geophys. Res. Lett.*, *30*(3), 1140, doi:10.1029/2002GL016291.
Gentemann, C. L., F. J. Wentz, M. Brewer, K. Hilburn, and D. Smith (2010), Passive microwave remote sensing of the ocean: An overview, in *Oceanography from Space*, edited by V. Barale, J. F. R. Gower, and L. Alberotanza, pp. 13–33, Springer, Netherlands.
Gordon, A., R. F. Weiss, W. M. Smethie and M. J. Warner (1992), Thermocline and intermediate water communication between the South Atlantic and Indian oceans, *J. Geophys. Res.*, *97*(C5), 7223–7240, doi:10.1029/92JC00485.
Goubanova, K., S. Illig, E. Machu, V. Garçon, and B. Dewitte (2013), SST subseasonal variability in the central Benguela upwelling system as inferred from satellite observations (1999–2009), *J. Geophys. Res. Oceans*, *118*, 4092–4110, doi:10.1002/jgrc.20287.
Gutknecht, E., et al. (2013), Nitrogen transfers off Walvis Bay: A 3-D coupled physical/biogeochemical modeling approach in the Namibian upwelling system, *Biogeosciences*, *10*(6), 4117–4135, doi:10.5194/bg-10-4117-2013.
Haidvogel, D. B., H. G. Arango, K. Hedstrom, A. Beckmann, P. Malanotte-Rizzoli, and A. F. Shchepetkin (2000), Model evaluation experiments in the North Atlantic Basin: Simulations in nonlinear terrain-following coordinates, *Dyn. Atmos. Oceans*, *32*(3–4), 239–281, doi:10.1016/S0377-0265(00)00049-X.
Hormazabal, S., G. Shaffer, and O. Pizarro (2002), Tropical Pacific control of intraseasonal oscillations off Chile by way of oceanic and atmospheric pathways, *Geophys. Res. Lett.*, *29*(6), 1081, doi:10.1029/2001GL013481.
Houry, S., E. Dombrowsky, P. De Mey, and J.-F. Minster (1987), Brunt-Väisälä frequency and Rossby radii in the South Atlantic, *J. Phys. Oceanogr.*, *17*(10), 1619–1626, doi:10.1175/1520-0485.
Hu, Z.-Z., and B. Huang (2007), Physical processes associated with the tropical Atlantic SST gradient during the anomalous evolution in the southeastern ocean, *J. Clim.*, *20*(14), 3366–3378, doi:10.1175/JCLI4189.1.
Huang, B., P. S. Schopf, and J. Shukla (2004), Intrinsic ocean–atmosphere variability of the tropical Atlantic Ocean, *J. Clim.*, *17*(11), 2058–2077, doi:10.1175/1520-0442.
Illig, S., and B. Dewitte (2006), Local coupled equatorial variability versus remote ENSO forcing in an intermediate coupled model of the tropical Atlantic, *J. Clim.*, *19*(20), 5227–5252.
Illig, S., B. Dewitte, N. Ayoub, Y. du Penhoat, G. Reverdin, P. De Mey, F. Bonjean, and G. S. E. Lagerloef (2004), Interannual long equatorial waves in the tropical Atlantic from a high-resolution ocean general circulation model experiment in 1981-2000, *J. Geophys. Res.*, *109*, C02022, doi:10.1029/2003JC001771.
Illig, S., D. Gushchina, B. Dewitte, N. Ayoub, and Y. du Penhoat (2006), The 1996 equatorial Atlantic warm event: Origin and mechanisms, *Geophys. Res. Lett.*, *33*, L09701, doi:10.1029/2005GL025632.
Illig, S., B. Dewitte, K. Goubanova, G. Cambon, J. Boucharel, F. Monetti, C. Romero, S. Purca, and R. Flores (2014), Forcing mechanisms of intraseasonal SST variability off central Peru in 2000-2008, *J. Geophys. Res. Oceans*, *119*, 3548–3573, doi:10.1002/2013JC009779.
Kalnay, E., et al. (1996), The NCEP/NCAR 40-year reanalysis project, *Bull. Am. Meteorol. Soc.*, *77*(3), 437–471, doi:10.1175/1520-0477.
Kanamitsu, M., W. Ebisuzaki, J. Woollen, S.-K. Yang, J. J. Hnilo, M. Fiorino, and G. L. Potter (2002), NCEP–DOE AMIP-II Reanalysis (R-2), *Bull. Am. Meteorol. Soc.*, *83*(11), 1631–1643, doi:10.1175/BAMS-83-11-1631.
Katz, E. J. (1997), Waves along the equator in the Atlantic*, *J. Phys. Oceanogr.*, *27*(12), 2536–2544, doi:10.1175/1520-0485.
Kessler, W. S., M. J. McPhaden, and K. M. Weickmann (1995), Forcing of intraseasonal Kelvin waves in the equatorial Pacific, *J. Geophys. Res.*, *100*(C6), 10,613–10,631, doi:10.1029/95JC00382.
Kummerow, C., et al. (2000), The status of the tropical rainfall measuring mission (TRMM) after two years in orbit, *J. Appl. Meteorol.*, *39*(12), 1965–1982, doi:10.1175/1520-0450.
Kuypers, M. M. M., G. Lavik, D. Woebken, M. Schmid, B. M. Fuchs, R. Amann, B. B. Jørgensen, and M. S. M. Jetten (2005), Massive nitrogen loss from the Benguela upwelling system through anaerobic ammonium oxidation, *Proc. Natl. Acad. Sci. U.S. A.*, *102*(18), 6478–6483, doi:10.1073/pnas.0502088102.
Large, W., J. Mcwilliams, and S. Doney (1994), Oceanic vertical mixing: A review and a model with a nonlocal boundary-layer parameterization, *Rev. Geophys.*, *32*(4), 363–403, doi:10.1029/94RG01872.
Lavik, G., et al. (2009), Detoxification of sulphidic African shelf waters by blooming chemolithotrophs, *Nature*, *457*(7229), 581–584, doi:10.1038/nature07588.
Lemarié, F., J. Kurian, A. F. Shchepetkin, M. J. Molemaker, F. Colas, and J. C. McWilliams (2012), Are there inescapable issues prohibiting the use of terrain-following coordinates in climate models?, *Ocean Modell.*, *42*, 57–79, doi:10.1016/j.ocemod.2011.11.007.
Leth, O., and J. F. Middleton (2006), A numerical study of the upwelling circulation off central Chile: Effects of remote oceanic forcing, *J. Geophys. Res.*, *111*, C12003, doi:10.1029/2005JC003070.
Le Traon, P. Y., F. Nadal, and N. Ducet (1998), An improved mapping method of multisatellite altimeter data, *J. Atmos. Oceanic Technol.*, *15*(2), 522–534, doi:10.1175/1520-0426.

Liu, W. T., W. Q. Tang, and P. S. Polito (1998), NASA scatterometer provides global ocean-surface wind fields with more structures than numerical weather prediction, *Geophys. Res. Lett.*, *25*(6), 761–764, doi:10.1029/98GL00544.
Lübbecke, J. F., C. W. Böning, N. S. Keenlyside, and S.-P. Xie (2010), On the connection between Benguela and equatorial Atlantic Niños and the role of the South Atlantic Anticyclone, *J. Geophys. Res.*, *115*, C09015, doi:10.1029/2009JC005964.
Lutjeharms, J. R. E. and R. C. Van Ballegooyen (1988), The Retroflection of the Agulhas Current, *J. Phys. Oceanogr.*, *18*, 1570–1583.
Marchesiello, P., J. C. Mc Williams, and A. F. Shchepetkin (2001), Open boundary conditions for long-term integration of regional ocean models, *Ocean Modell.*, *3*, 1–20.
Marchesiello, P., L. Debreu, and X. Couvelard (2009), Spurious diapycnal mixing in terrain-following coordinate models: The problem and a solution, *Ocean Modell.*, *26*(3–4), 156–169, doi:10.1016/j.ocemod.2008.09.004.
Marin, F., G. Caniaux, H. Giordani, B. Bourlès, Y. Gouriou, and E. Key (2009), Why were sea surface temperatures so different in the eastern equatorial Atlantic in June 2005 and 2006?, *J. Phys. Oceanogr.*, *39*(6), 1416–1431, doi:10.1175/2008JPO4030.1.
Melsom, A., S. D. Meyers, J. J. O'Brien, H. E. Hurlburt, and J. E. Metzger (1999), ENSO effects on gulf of Alaska eddies, *Earth Interact.*, *3*(1), 1–30, doi:10.1175/1087-3562.
Mosquera-Vásquez, K., B. Dewitte and S. Illig (2014), The central Pacific El Niño intraseasonal Kelvin wave, *J. Geophys. Res. Oceans*, *119*, 6605–6621, doi:10.1002/2014JC010044.
Penven, P., C. Roy, J. R. E. Lutjeharms, A. Colin de Verdière, A. Johnson, F. Shillington, P. Freon and G. Brundrit (2001), A regional hydrodynamic model of upwelling in the Southern Benguela, *S. Afr. J. Sci.*, *97*, 472–475.
Penven, P., V. Echevin, J. Pasapera, F. Colas, and J. Tam (2005), Average circulation, seasonal cycle, and mesoscale dynamics of the Peru Current System: A modeling approach. *J. Geophys. Res.*, *110*, C10021, doi:10.1029/2005JC002945.
Penven, P., L. Debreu, P. Marchesiello, and J. C. McWilliams (2006a), Evaluation and application of the ROMS 1-way embedding procedure to the central California upwelling system, *Ocean Modell.*, *12*(1–2), 157–187, doi:10.1016/j.ocemod.2005.05.002.
Penven, P., J. R. E. Lutjeharms, and P. Florenchie (2006b), Madagascar: A pacemaker for the Agulhas current system?, *Geophys. Res. Lett.*, *33*, L17609, doi:10.1029/2006GL026854.
Penven, P., P. Marchesiello, L. Debreu and J. Lefevre (2008), Software tools for pre- and post-processing of oceanic regional simulations, *Environ. Modell. Software*, *23*, 660–662.
Philander, S. G. H. (1986), Unusual conditions in the tropical Atlantic Ocean in 1984, *Nature*, *322*(6076), 236–238, doi:10.1038/322236a0.
Pizarro, O., A. J. Clarke, and S. Van Gorder (2001), El Niño sea level and currents along the south American coast: Comparison of observations with theory, *J. Phys. Oceanogr.*, *31*(7), 1891–1903, doi:10.1175/1520-0485.
Pizarro, O., G. Shaffer, B. Dewitte, and M. Ramos (2002), Dynamics of seasonal and interannual variability of the Peru-Chile Undercurrent, *Geophys. Res. Lett.*, *29*(12), 1581, doi:10.1029/2002GL014790.
Polo, I., A. Lazar, B. Rodriguez-Fonseca, and S. Arnault (2008), Oceanic Kelvin waves and tropical Atlantic intraseasonal variability: 1. Kelvin wave characterization, *J. Geophys. Res.*, *113*, C07009, doi:10.1029/2007JC004495.
Reason, C. J. C., P. Florenchie, M. Rouault, and J. Veitch (2006), Influences of large scale climate modes and agulhas system variability on the BCLME region, in *Large Marine Ecosystems*, vol. 14, chap. 10, edited by G. Hempel et al., pp. 223–238, Elsevier, Amsterdam, Netherlands.
Richter, I., S. K. Behera, Y. Masumoto, B. Taguchi, N. Komori, and T. Yamagata (2010), On the triggering of Benguela Niños: Remote equatorial versus local influences, *Geophys. Res. Lett.*, *37*, L20604, doi:10.1029/2010GL044461.
Ridgway, K. R., J. R. Dunn, and J. L. Wilkin (2002), Ocean interpolation by four-dimensional weighted least squares: Application to the waters around Australasia, *J. Atmos. Oceanic Technol.*, *19*(9), 1357–1375, doi:10.1175/1520-0426.
Romea, R. D., and R. L. Smith (1983), Further evidence for coastal trapped waves along the Peru Coast, *J. Phys. Oceanogr.*, *13*(8), 1341–1356, doi:10.1175/1520-0485.
Rouault, M., P. Florenchie, N. Fauchereau, *and* C. J. C. Reason *(2003)* South East tropical Atlantic warm events and southern African rainfall, *Geophys. Res. Lett.*, *30*(5), 8009, doi:10.1029/2002GL014840
Rouault, M., S. Illig, C. Bartholomae, C. J. C. Reason, and A. Bentamy (2007), Propagation and origin of warm anomalies in the Angola Benguela upwelling system in 2001, *J. Mar. Syst.*, *68*(3–4), 473–488, doi:10.1016/j.jmarsys.2006.11.010.
Rouault, M., J. Servain, C. J. C. Reason, B. Bourlès, M. J. Rouault, and N. Fauchereau (2009), Extension of PIRATA in the tropical South-East Atlantic: An initial one-year experiment, *Afr. J. Mar. Sci.*, *31*(1), 63–71, doi:10.2989/AJMS.2009.31.1.5.776.
Saha, S., et al. (2010), The NCEP climate forecast system reanalysis, *Bull. Am. Meteorol. Soc.*, *91*(8), 1015–1057, doi:10.1175/2010BAMS3001.1.
Schouten, M. W., R. P. Matano, and T. P. Strub (2005), A description of the seasonal cycle of the equatorial Atlantic from altimeter data, *Deep Sea Res. Part I*, *52*(3), 477–493, doi:10.1016/j.dsr.2004.10.007.
Shaffer, G., O. Pizarro, L. Djurfeldt, S. Salinas, and J. Rutllant (1997), Circulation and low-frequency variability near the Chilean Coast: Remotely forced fluctuations during the 1991–92 El Niño, *J. Phys. Oceanogr.*, *27*(2), 217–235, doi:10.1175/1520-0485.
Shannon, L. V. (1985), The Benguela ecosystem. 1. Evolution of the Benguela, physical features and processes, in *Oceanography and Marine Biology: An Annual Review*, vol. 23, edited by M. Barnes, pp.105–182, Aberdeen Univ. Press, Aberdeen, U. K.
Shannon, L. V., and G. Nelson (1996), The Benguela: Large scale features and processes and system variability, in *The South Atlantic Past and Present Circulation*, edited by G. Wefer et al., pp. 163–210, Springer, Berlin, Germany.
Shannon, L. V., A. J. Boyd, G. B. Brundrit, and J. Taunton-Clark (1986), On the existence of an El Niño-type phenomenon in the Benguela system, *J. Mar. Res.*, *44*(3), 495–520, doi:10.1357/002224086788403105.
Shannon, V., G. Hempel, C. Moloney, J. D. Woods, and P. Malanotte-Rizzoli (2006), *Benguela: Predicting a Large Marine Ecosystem: Predicting a Large Marine Ecosystem*, Elsevier, Amsterdam, Netherlands.
Shchepetkin, A. F., and J. C. McWilliams (2003), A method for computing horizontal pressure-gradient force in an oceanic model with a nonaligned vertical coordinate, *J. Geophys. Res.*, *108*(C3), 3090, doi:10.1029/2001JC001047.
Shchepetkin, F. A., and J. C. McWilliams (2005), The regional oceanic modeling system (ROMS): A split-explicit, free-surface, topography-following-coordinate oceanic model, *Ocean Modell.*, *9*(4), 347–404, doi:10.1016/j.ocemod.2004.08.002.
Shillington, F.A. (1998), The Benguela upwelling system off southwestern Africa, in *The Sea, vol. 11, The Global Coastal Ocean, Regional Studies and Syntheses*, edited by A. R. Robinson and K. H. Brink, pp. 583–604, John Wiley, N. Y.
Shillington, F. A., C. J. C. Reason, C. M. Duncombe-Rae, P. Florenchie, and P. Penven (2006), Large scale physical variability of the Benguela Current large marine ecosystem (BCLME), in *Benguela: Predicting a Large Marine Ecosystem, Large Marine Ecosystems*, vol. 14, edited by V. Shannon et al., pp. 49–70, Elsevier, Amsterdam.
Strub, P. T., J. M. Mesias, V. Montecino-B., J. Rutllant-C. and S. Salinas-M. (1998), *Coastal ocean circulation off western South America, The Sea, 11*, edited by A.R. Robinson, and K.H. Brink, pp. 273–313, John Wiley and Sons, N. Y.

Taylor, K. E. (2001), Summarizing multiple aspects of model performance in a single diagram, *J. Geophys. Res.*, *106*(D7), 7183–7192, doi:10.1029/2000JD900719.

Torrence, C., and G. P. Compo (1998), A practical guide to wavelet analysis, *Bull. Am. Meteorol. Soc.*, *79*(1), 61–78, doi:10.1175/1520-0477.

Toumazou, V., and J.-F. Cretaux (2001), Using a Lanczos eigen solver in the computation of empirical orthogonal functions, *Mon. Weather Rev.*, *129*(5), 1243–1250, doi:10.1175/1520-0493.

Veitch, J., P. Penven, and F. Shillington (2009), The Benguela: A laboratory for comparative modeling studies, *Prog. Oceanogr.*, *83*(1), 296–302, doi:10.1016/j.pocean.2009.07.008.

Wilson, C., and D. Adamec (2002), A global view of bio-physical coupling from SeaWiFS and TOPEX satellite data, 1997–2001, *Geophys. Res. Lett.*, *29*(8), 1257, doi:10.1029/2001GL014063.

Zabel, M., et al. (2003), *Report and Preliminary Results of METEOR Cruise M 57/2, Walvis Bay - Walvis Bay, 11.02.−12.03.2003*, Dep. Geosci., Bremen Univ., Bremen, Germany.

Zamudio, L., A. P. Leonardi, S. D. Meyers, and J. J. O'Brien (2001), ENSO and eddies on the southwest coast of Mexico, *Geophys. Res. Lett.*, *28*(1), 13–16, doi:10.1029/2000GL011814.

Zamudio, L., H. E. Hurlburt, E. J. Metzger, S. L. Morey, J. J. O'Brien, C. Tilburg, and J. Zavala-Hidalgo (2006), Interannual variability of Tehuantepec eddies, *J. Geophys. Res.*, *111*, C05001, doi:10.1029/2005JC003182.

Zamudio, L., H. E. Hurlburt, E. J. Metzger, and C. E. Tilburg (2007), Tropical wave-induced oceanic eddies at Cabo Corrientes and the Maria Islands, Mexico, *J. Geophys. Res.*, *112*, C05048, doi:10.1029/2006JC004018.

Zebiak, S. E. (1993), Air-sea interaction in the equatorial Atlantic region, *J. Clim.*, *6*(8), 1567–1586, doi:10.1175/1520-0442.